https://ntrs.nasa.gov/search.jsp?R=19770016110 2018-07-25T01:16:43+00:00Z

# General Disclaimer

## One or more of the Following Statements may affect this Document

- This document has been reproduced from the best copy furnished by the organizational source. It is being released in the interest of making available as much information as possible.

- This document may contain data, which exceeds the sheet parameters. It was furnished in this condition by the organizational source and is the best copy available.

- This document may contain tone-on-tone or color graphs, charts and/or pictures, which have been reproduced in black and white.

- This document is paginated as submitted by the original source.

- Portions of this document are not fully legible due to the historical nature of some of the material. However, it is the best reproduction available from the original submission.

Produced by the NASA Center for Aerospace Information (CASI)

CR 151999

(NASA-CR-151999) COMPUTATION OF VISCOUS TRANSONIC FLOW ABOUT A LIFTING AIRFOIL (Numerical Continuum Mechanics, Inc.) 93 p HC A05/MF A01 CSCL 01A

N77-23054

Unclas

G3/02 28870

MAY 1977
RECEIVED
NASA STI FACILITY
INPUT BRANCH

NASA CR-151999

NCMR-76-100

# COMPUTATION OF VISCOUS TRANSONIC FLOW ABOUT A LIFTING AIRFOIL

Prepared by:

L. Walitt
C.Y. Liu

for

AMES RESEARCH CENTER

National Aeronautics and Space Administration
Moffett Field, California 94035

The work reported herein was
performed under Contract NAS2-9052

November 1976

Numerical Continuum Mechanics, Inc.
6269 Variel Avenue, Suite 200
Woodland Hills, California 91367

ACKNOWLEDGEMENTS

The authors are pleased to acknowledge the contributions of Mr. L. S. King of NASA AMES Research Center and Ms. J. A. Enos of Computer Sciences Corporation to the work reported herein. Mr. King developed the original computer program, which was the starting point for this study, derived the characteristic boundary condition equations employed at the downstream boundary, and provided many helpful suggestions and discussions in the course of this work. Ms. Enos vectoized the computer code employed in this study, generated some of the plots used, and provided programming support throughout this development effort.

TABLE OF CONTENTS


| SECTION | | PAGE |
|---|---|---|
| | ABSTRACT | iii |
| | NOMENCLATURE | iv |
| 1. | INTRODUCTION | 2 |
| 2. | THE STOKES CODE | 6 |
| | 2.1 Switched Axis Computation | 7 |
| | 2.2 Vector Do Loops | 8 |
| | 2.3 Multi-regional Timesteps | 9 |
| 3. | TURBULENCE AND TRANSITION MODELS | 12 |
| | 3.1 Turbulence Modelling | 12 |
| | 3.2 Algebraic Turbulence Models | 14 |
| | 3.3 Transition to Turbulence | 19 |
| 4. | BOUNDARY CONDITIONS FOR NON-LIFTING AND LIFTING AIRFOILS | 21 |
| | 4.1 Non-Lifting Airfoil | 21 |
| | 4.2 Lifting Airfoil | 23 |
| 5. | RESULTS OF NON-LIFTING CALCULATION | 27 |
| | 5.1 Mesh Used and Initial Conditions | 27 |
| | 5.2 Time-Histories of Pressure Coefficients | 29 |
| | 5.3 Computational Time Reduction Factor | 30 |
| | 5.4 Velocity Vectors of Steady Flow Field | 31 |
| | 5.5 Surface Pressure Distribution Comparisons | 32 |
| | 5.6 Mach Number Contours | 33 |
| 6. | RESULTS OF LIFTING CALCULATION | 34 |
| | 6.1 Finite Difference Mesh | 34 |
| | 6.2 Initial Conditions | 35 |
| | 6.3 Computational Time Reduction Factor | 36 |
| | 6.4 General Flow Field Structure | 39 |
| | 6.5 Calculated Lift and Drag | 40 |
| | 6.6 Integrated Inviscid/Viscous Calculation | 42 |
| | 6.6.1 General Flow Field Structure | 43 |
| | 6.6.2 Calculated Lift and Drag | 44 |
| | 6.6.3 Surface Pressure Distribution Comparison | 46 |
| | 6.6.4 Comparison of Mach Number Contours | 48 |
| | 6.6.5 Turbulence Characteristics for Airfoil | 49 |
| 7. | CONCLUSIONS AND RECOMMENDATION | 51 |
| 8. | REFERENCES | 53 |

## ABSTRACT

Results are presented from a numerical investigation of the viscous transonic flow about a stationary body in free air. The geometry chosen was a symmetric NACA 64A010 airfoil at a freestream Mach number of 0.8, a Reynolds number of 4 million based on chord, and angles of attack of 0 and 2 degrees. These conditions were such that, at 2 degrees incidence unsteady periodic motion was calculated along the aft portion of the airfoil and in its wake. This unsteady phenomenon has been experimentally observed for other airfoil geometries at transonic speeds. Although no unsteady measurements were made for the NACA 64A010 airfoil at these flow conditions, interpolated steady measurements of lift, drag, and surface static pressures compared favorably with corresponding computed time-averaged lift, drag, and surface static pressures.

## NOMENCLATURE

| | |
|---|---|
| $a$ | Local Sound Speed |
| $A$ | Surface Area |
| $C_x$ | Particle chord length |
| $C$ | Chord |
| $C_D$ | Drag coefficient, $\frac{\text{drag force}}{q_\infty C}$ |
| $C_L$ | Lift coefficient, $\frac{\text{lift force}}{q_\infty C}$ |
| $C_p$ | Pressure coefficient, $(p-p_\infty)/q_\infty$ |
| $C_p$ | Specific heat at constant pressure |
| $C_v$ | Specific heat at constant volume |
| $D$ | Area of airfoil section |
| $E$ | Specific internal energy |
| $H$ | Stagnation enthalpy |
| $K$ | Reduced frequency, $\omega C/U_\infty$ |
| $K$ | Transonic Parameter, $(1-M_\infty^2)/M_\infty \delta^{2/3}$ |
| $\ell$ | Mixing length |
| $m$ | Mass |
| $M$ | Mach number |
| $N$ | Cycle number |
| $p$ | Pressure |
| $q$ | Dynamic Pressure, $\frac{1}{2}\rho U^2$ |
| $\bar{r}$ | Transformed radius, $(\bar{x}^2 + K\bar{y}^2)^{\frac{1}{2}}$ |

| | |
|---|---|
| $Re$ | Reynolds number |
| $Re_\theta$ | Reynolds number based on momentum thickness |
| $Re_x$ | Reynolds number based on x |
| $Re_c$ | Reynolds number based on chord |
| $S$ | Entropy |
| $t$ | Time |
| $\Delta t$ | Timestep |
| $T$ | Temperature |
| $u$ | Velocity component in x direction |
| $U_\infty$ | Freestream Velocity |
| $v$ | Velocity component in y direction |
| $V$ | Volume |
| $x$ | Streamwise coordinate |
| $\underset{\sim}{x}$ | Non-dimensional coordinate, $x/(c/2)$ |
| $y$ | Normal coordinate |
| $\underset{\sim}{y}$ | Non-Dimensional coordinate, $y/(c/2)$ |
| $\tilde{y}$ | Scaled transonic parameter, $\delta^3 M_\infty^{\frac{1}{2}} \underset{\sim}{y}$ |
| $\alpha$ | Angle of attack |
| $\gamma$ | Ratio of specific heats |
| $\Gamma$ | Circulation |
| $\delta$ | Boundary layer thickness |
| $\delta$ | Airfoil thickness to chord ratio, $t/c$ |
| $\epsilon$ | Eddy viscosity |
| $\epsilon$ | Small disturbance parameter, $\delta^{2/3}/M_\infty$ |
| $\theta$ | Transformed angle, $\tan^{-1}(\tilde{y} K^{\frac{1}{2}}/\underset{\sim}{x})$ |
| $\theta$ | Momentum thickness |

| | |
|---|---|
| $\mu$ | Molecular viscosity |
| $\nu$ | Kinematic viscosity |
| $\rho$ | Density |
| $\tau$ | Shear Stress |
| $\tau$ | Maximum thickness of airfoil |
| $\tau$ | Characteristic Time, $tU_\infty/c$ |
| $\phi$ | Velocity potential function |
| $\phi'$ | Transformed velocity potential function |
| $\phi_0'$ | Doublet potential |
| $(\ )_\infty$ | Freestream condition |
| $(\underset{\sim}{\ })$ | Non-dimensional coordinate |
| $(\tilde{\ })$ | Scaled coordinate |
| $(\ )_{\underset{\sim}{x}}$ | Derivative with respect to parameter $\underset{\sim}{x}$ |
| $(\ )_{\underset{\sim}{y}}$ | Derivative with respect to parameter $\underset{\sim}{y}$ |
| $(\ )_{\tilde{\eta}}$ | Derivative with respect to parameter $\tilde{\eta}$ |
| $(\bar{\ })$ | Time-averaged property |
| $(\ )_w$ | Wall quanitiy |

## SECTION 1

## INTRODUCTION

The principal objective of this research effort is to numerically calculate the viscous transonic flow field about a stationary lifting airfoil in free air. To our knowledge, this calculation represents the first-of-a-kind in transonic aerodynamics.

Previous transonic lifting airfoil computations concerned steady inviscid flow with varying degrees of approximation to the Euler's equations. For example, Murman and Cole (Ref. 1), Krupp and Murman (Ref. 2), and more recently Murman, Bailey, and Johnson (Ref. 3) solved the transonic small disturbance equation for flow past thin airfoils including imbedded shock waves. Transonic small disturbance theory solves the small perturbation equation (Ref. 4) with an approximate tangency condition at the airfoil surface, and under the assumption of isentropic flow. Jameson solved the transonic full potential equation (Ref. 5) using an exact tangency condition at the airfoil surface, and under the isentropic assumption (Ref. 6). Furthermore, Jameson's method permits computation of imbedded shocks.

Magnus and Yoshihara (Ref. 7) solved the unsteady form of the Euler equations through an explicit finite difference scheme. A numerical solution of Euler's equations, including the possibility of embedded shocks (through shock capturing), embodies no other assumptions but the inviscid flow assumption. Coincident with the inviscid assumption, all three methods cited above employ a Kutta condition to determine the magnitude of the circulation for lifting bodies.

For a lifting transonic airfoil with little or no separation in the neighborhood of the shock, combination of turbulent boundary layer theory (Refs. 8 and 9) with any of the above inviscid methods yields useful predictions of the shock location, lift coefficient, and drag coefficient, provided that a displacement thickness correction is made to the airfoil shape. However, when the shock wave boundary layer interaction induces considerable flow separation,



PRECEDING PAGE BLANK NOT FILMED

integrated inviscid-boundary layer theories are of dubious value in prediction of the shock location, lift, and drag of the system. Liepman and Roshko (Ref. 10) point out that transonic shock-wave boundary layer interactions involve an interplay between strength and position of shock waves on the body and boundary layer character, i.e., separation. The complete equations of motion are thus needed to properly account for these nonlinear interactions.

Numerical solution of the time-dependent Navier-Stokes equations, including turbulence and transition via models, yields predictions of the shock location, lift coefficient, and drag coefficient of an airfoil under conditions of considerable flow separation. Thus, for thick transonic airfoils at moderate angles of attack, or for thin transonic airfoils at high angles of attack, numerical solution to the time-dependent Navier-Stokes equations is the only means for flow field prediction.

A time-dependent Navier-Stokes calculation does not invoke a Kutta condition at the airfoil trailing edge, and includes viscous effects; hence, the possibility of vortex shedding, with attendent periodic flow is within the scope of this computation. For example, McDevitt, Levy, and Deiwert (Ref. 11) and Finke (Ref. 12) measured unsteady periodic flow about transonic airfoils for a limited range of Mach numbers and angles-of-attack. Finke's experiments on a symmetric NACA $63_1$ -012 airfoil at Mach .70, Reynolds number $1.25 \times 10^6$ based on chord, and two degrees incidence, show periodic flow at the airfoil trailing edge with a reduced frequency* K of 2.5 for the oscillating shock. The amplitide of shock oscillation is about one percent of the chord at two degrees angle of attack and increases to 10% of the chord at eight degrees incidence.

* The reduced frequency K is defined as the product of the angular frequency and the chord divided by the free stream velocity.

Finke (Ref. 12) also took interferogram pictures over one full period of shock oscillation for a quasi-elliptical NRL-profile, at a Mach number of .71, a Reynolds number based on chord of $1 \times 10^6$, and at 5 degrees angle of attack. These interferogram pictures, which represent lines of constant density, are shown in Figure 1. The pictures are depicted in intervals of 700 $\mu$s. In picture 3, the shock is positioned at 40 percent chord, in picture 5 the shock degenerates to a Mach wave and leading-edge separation determines the flow. Finally, picture 8 is similar to picture 2 indicating periodic flow. Shedding of vorticity is also indicated in the pictures of Figure 1.

The geometry for this investigation was a symmetric NACA 64A010 airfoil at a freestream Mach number of .80, a Reynolds number of $4 \times 10^6$ based on chord, and at angles of attack of 0 and 2 degrees. At 2 degrees incidence unsteady periodic motion was calculated along the aft portion of the airfoil and in its wake. Although no unsteady measurements were made for the NACA 64A010 airfoil at these flow conditions, interpolated steady measurements of lift, drag, and surface static pressures compared favorably with corresponding computed time-averaged lift, drag, and surface static pressures.

In order to solve for the unsteady viscous transonic flow field about a lifting body in free air, research was conducted in three principal areas. The are as follows:

1. A computer code, called "STOKES", was developed which solved the Navier-Stokes equations with Multi-Regional Timesteps (MRT) and Vector-Do-Loops (VDL). The MRT/VDL logic significantly reduced computational time.

2. Turbulence and transition models were incorporated into the STOKES computer code.

3. Boundary conditions were generated along the perimeter of the region of calculation which simulated the lifting airfoil immersed in a free airstream.

A discussion of the STOKES computer code is presented in Section 2, the turbulence and transition models embodied in the STOKES code are described in Section 3, boundary conditions are presented in Section 4, while results of the non-lifting ($\alpha = 0^\circ$) and lifting ($\alpha = 2^\circ$) airfoil calculations are discussed in Sections 5 and 6, respectively. Section 7 presents the conclusions reached in this research effort.

## SECTION 2

## THE STOKES CODE

A computer code has been developed, called "STOKES", for calculating viscous, compressible, time-dependent flow fields about two-dimensional aerodynamic bodies. This code solves the Navier-Stokes equations including turbulence, transition, and free air boundary conditions along the perimeter of the domain of calculation. The finite difference equations embodied in the STOKES code were originally developed by Trulio (Ref. 13). These finite difference analogs of the equations of motion are such that their self consistency property is maintained. That is, the finite difference equations for continuity, momenta, and internal energy imply an exact finite difference equation for total energy. The Trulio finite difference relations are second order accurate in space and first order accurate in time according to Taylor's series analysis.

Turbulence and transition are discussed in Section 3, while the free air boundary conditions are described in Section 4. This Section is concerned with the numerical method employed to solve the finite difference analogs of the equations of motion embodied in the STOKES code.

The principal innovation embodied in this computer code concerns computational time reduction. A method has been developed which produced computational time reduction factors between five and ten. For a non-lifting airfoil the flow field can be computed in less than 30 minutes on a CDC 7600 computer, while for a lifting airfoil the calculation requires less than two hours.

The STOKES computer code employs three principal time-reduction methods.

1. Writing the program to proceed along quasi-streamlines rather than the conventional processing along potential-like lines.

2. Incorporation of special assembly language subroutines to take maximal advantage of the "pipelining" capability of the more advanced computers.
3. Setting up a procedure whereby the computational domain is automatically divided into several regions in which different timesteps govern numerical stability.

## 2.1 Switched Computational Axis

Let us consider computation of the flow field about a two-dimensional body whose axis is parallel to the x coordinate axis, and immersed in an airstream moving along the x-axis.. The y-coordinate is considered the normal direction. The computation takes place on a finite difference mesh comprised of the intersection of quasi-streamlines, which are nearly parallel to the x-axis and extend upstream to downstream, and potential-like lines, which are nearly paralled to the y-axis, and initiate below the body and end above the body.

Due to computer storage limitations, computations were previously conducted along the potential-like lines of the mesh, starting from the line farthest upstream of the body and ending at the line farthest downstream of the body. This mode of computation is referred to as unswitched. Usually the potential-like lines are shorter than the quasi-streamlines; hence, they are comprised of fewer points. With fewer points to a calculational line the do-loops in the program are executed fewer times, and there are correspondingly more interruptions for data transfer between central and peripheral memory banks. Furthermore, most potential-like lines of the finite difference mesh pass through the body; hence, special branch point logic is required to account for the body aerodynamics.

The switched axis computer code performs computations along the streamline-like lines of the finite difference mesh rather than along the potential-like lines. For each calculational line the do-loops in the program are executed a greater number of times and the number of data transfer interruptions are reduced. Furthermore, the body geometry becomes two special streamlines of the mesh in the switched mode of computation. Through most of the streamline computational sweeps there is no branching of logic. For the above reasons, the switched axis mode of computation is more efficient than the unswitched mode (Ref. 14).

## 2.2 The Vector Do-Loop

Recently at NASA-Ames Research Center, Dr. H. Lomax started development of CDC 7600 assembly language subroutines to replace operations done in regular FORTRAN do-loops. These subroutines were designated "Vector Do-Loops," i.e., VDL*. The Vector-Do-Loop takes advantage of the instruction stack of the CDC 7600 computer and employs the concept of pipeling in the computational sequence. In Reference 14, a simple vector do-loop is explained and an actual example is given showing the speed-up factor between a vector do-loop subroutine and the equivalent FORTRAN program.

The Vector-Do-Loop substitutes computation during the waiting periods that normally occur in FORTRAN do-loops. The case of the vector routine is a tight loop with computations going on at different stages of development, while the FORTRAN Do-Loop is essentially a series calculation. The Vector-Do-Loop fits into the instruction stack and thus executes quickly. By making optimal use of the CPU registers, the Vector-Do-Loop can do the work of a FORTRAN-Do-Loop faster and more efficiently.

* The vector do-loops have also been referred to as the SSPEEDY Codes.

## 2.3 Multi-Regional Timesteps

The Multi-Regional-Timestep (MRT) logic divides the domain of computation into a set of concentric regions about the airfoil. In each concentric region a different timestep is employed, which is governed by the stability of that particular region. The timestep generally increases by a factor of two as one moves from the inner concentric region towards the outer one. Thus, the inner regions are calculated frequently, while the outer regions are calculated infrequently.

The MRT logic embodied in the STOKES computer code is based on concepts developed by Magnus and Yoshihara (Refs. 7 and 15) and Trulio (Refs. 16 and 17). In solving for the inviscid field about an oscillating airfoil (Ref. 15), Magnus and Yoshihara employed four concentric mesh regions about the airfoil. Three are employed in the vicinity of the airfoil nose and the fourth is a coarse cartesian mesh which contains the other three and covers the remainder of the domain of calculation. The three in the nose region are a fine skewed mesh adjacent to the airfoil, a fine cartesian mesh containing the skewed mesh, and a medium cartesian mesh containing the other two. In their explicit differencing scheme the allowable timestep is limited by stability criteria to an amount which is directly proportional to the spatial mesh increments. For each explicit timestep advancing the solution in the coarsest cartesian mesh of the system, 8 are made in the medium cartesian mesh, 64 are made in the fine cartesian mesh, and 256 are made in the skewed elliptic mesh around the nose. Thus, Magnus and Yoshihara employed four concentric regions in their computation of flow about an oscillating airfoil.

The multi-regional timestip formulation employed herein is patterned after that of Magnus and Yoshihara. A set of concentric regions is developed each of which extends from the upstream to the downstream boundary and contains the airfoil. In this formulation, which takes

place in the switched axis computer code , the variables of motion are calculated for a given layer of zones as often as required by considerations of stability of that layer of zones and its immediate neighbors, rather than the former method of updating dependent variables for all zones as often as required for the least stable zone of the finite difference mesh. Since the finite difference mesh is composed of streamline-like lines finely spaced in the neighborhood of a surface and coarsely spaced as one moves away from the surface, there are many different timestep levels in a typical aerodynamic problem. Therefore, a high percentage of the zones, i.e., those in the large timestep levels, will be calculated very infrequently and great savings is computational time should occur.

The finite difference mesh is broken up into a series of regions comprised of a group of streamline-like lines. The regions are determined by stability for the least stable zone along a given streamline. The timestep levels monotonically decrease as one approaches the aerodynamic body from below, and the timestep levels monotonically increase as one moves away from the top surface of the aerodynamic body. In the multi-regional timestep approach, one-dimensional variable timestep techniques are employed to sove a two-dimensional problem. Some of the techniques published by Trulio (Refs. 16, 17) are incorporated in the multi-regional timestep approach considered herein. Particularly the concept of having adjacent concentric regions differ in timestep by a factor of two. Trulio has stated that under these conditions the conservation properties of the finite difference equations discussed in the introduction to Section 2 can be preserved after the solution is advanced in the coarsest region of the system.

Let us consider an airfoil finite difference mesh with four concentric regions, each differing by a factor of two in timestep, and let $\Delta t$ be the minimum timestep, a "microstep". It is required to update the variables of motion on this mesh through the total time

interval of 8 $\Delta t$, designated as a macro-step. The finest region will be updated through 8 increments in $\Delta t$, or through 8 "microsteps", the next finest region will be updated through 4 timesteps of 2 $\Delta t$, the medium region will be updated through 2 timesteps of 4 $\Delta t$ and the coarsest region through the macrostep.

Complexity is minimized relative to the generalized variable timestep procedure of Trulio (Refs. 14 and 16), since all points along a given streamline belong to the same timestep level. Hence, since the streamline spacing controls the timesteps in most two-dimensional problems, the simple multi-regional timestep approach should yield most of the benefits of a more complex general two-dimensional variable timestep method. Development of the MRT logic is presented in much more detail in Reference 18.

## SECTION 3

## TURBULENCE AND TRANSITION MODELS

An algebraic turbulence model, originally formulated by Baldwin and Rose (Ref. 19 ), is selected for the computation of turbulent flow over an airfoil at transonic speed. The model is, in effect, the mixing length theory to which relaxation along a streamline-like trajectory is incorporated. The simple algebraic model has been recently examined by Baldwin and Rose (Ref. 19 ), Deiwert (Ref. 20 ), and others to be useful in shock boundary-layer interaction problems. All versions of available algebraic models are discussed. A criterion for boundary layer transition is also presented.

### 3.1 Turbulence Modelling

Numerical modelling of turbulence has become quite practical in the past decade with the advancement of high-speed computers. Though a universal model with wide range of applicability is far from reality, there is ample evidence that existing models have served well even in complex situations such as shock-wave boundary-layer interaction. All models of turbulence are supposed to be general in scope, and until recently, cross-comparisons between models (mainly studies done at NASA-Ames, Refs. 19 , 20 , and 21 ) are few. For transonic flow, there is no definitive conclusion as to the best turbulence model to employ.

The usage of numerical models naturally bypasses the more fundamental approach to turbulence studies via statistical theory, which might be at times academically pleasing but unrealistic in engineering applications. In general, turbulence modelling is divided into two categories: the algebraic models such as mixing length theory, and the transport models which are described by one or more differential equations governing some quantity like turbulence energy, turbulence vorticity or shearing stress. The original work of Prandtl and its

subsequent extension by Cebeci and Smith (CS) (Refs. 22 and 23), Rose (Ref. 19), etc. are examples of the first class; the classical Kolmogorov model (Ref. 24) (1942) and the Saffman model (1970) (Ref. 25) fall into the latter category. In adopting a transport model, one must solve, in addition to the basic conservation laws, other differential equations from which turbulence stresses are determined. Transport models try to depict the physics of turbulence transport, generation, dissipation and diffusion. In addition, some models (such as Saffman's) show the correct analytical behavior near the wall (as demanded by the law of wall). The predictive capabilities for incompressible boundary layer flows by those models are convincingly established. Turbulent flows in more than two spatial dimensions, including separation, compressibility, rotational effects, and containing boundary layers interacting with shock waves have not been subject to examination by those models*. In short, the transport models, as promising as they are, have yet to be thoroughly tested by problems more complex than plane boundary layer flows.

In view of the existing complexities in the unsteady transonic flow problem, the desired economy in computation, and the added degree of complication in the nonlinear equations, we must see an alternative to the formulation by turbulence model equations. The alternative should be able to render a reasonably good description of the turbulent boundary layer development without a disproportional amount of computational time.

---

* Wilcox (Ref. 26), applying Saffman's model, has shown good results in the study of turbulent boundary separation and reattachment at moderate (2.96) Mach number.

## 3.2 Algebraic Turbulence Models

The mixing length theory, originated by Prandtl (Ref. 27), provides the foundation to all algebraic models. Modifications introduced by van Driest (Ref. 28), Cebeci and Smith (Refs. 22 and 23), and recently Baldwin and Rose (Ref. 19), Shang and Hankey (Ref. 29), and Deiwert (Ref. 20) all direct to improve the applicability of the model. Algebraic models bypass the necessity of solving additional differential equations. From a computational standpoint, the eddy viscosity based on an algebraic model is post processed from mean-flow information. Our past application of the CS mixing length theory to internal flow problems in an impeller has shown good qualitative results (Ref. 30). Quantitative comparison is not possible due to the complete lack of experimental data. Hence, some version of an algebraic turbulence model is prefered to the more complex transport model. Despite the mixing-length common ingredient, there are variations in each individual formulation. The variations range from the unmodified theory to a relaxation model incorporating special treatment for the separated regions. The relaxation model was found significantly better than the unmodified algebraic model. According to Shang and Hankey (Ref. 29), it was significantly better than the Saffman's transport model for flow over a flat plate. Since separation on the transonic airfoil is a real possibility, incorporation of the relaxation effect becomes quite desirable. For a detailed comparison of various formulations, we list them in the following table.

ORIGINAL PAGE IS
OF POOR QUALITY

$$\tau_{xy} = (\mu + \rho\epsilon)\left(\frac{\partial u}{\partial y} + \frac{\partial v}{\partial x}\right)$$

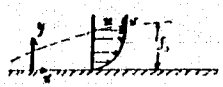


| | C-S Method | Rose-Balwin Baseline | Escudier | Rose-Balwin Relaxation | Shang & Hankey | Diewert Model ① | Diewert Model ② | Diewert Model ③ - Baseline | Diewert Model (4) - Relaxation |
|---|---|---|---|---|---|---|---|---|---|
| Inner region | $\epsilon_i = \ell_i^2 \left\lvert \frac{\partial u}{\partial y} \right\rvert$ where $\ell_i^2 = k_1^2 y^2 D^2$, $k_1 = 0.4$, $D = 1 - \exp(-\frac{y}{A})$, $A = 26\nu / \sqrt{\frac{\tau_w}{\rho} + \frac{dp}{dx}\frac{y}{\rho}}$ | $\epsilon_i = \ell_i^2 \left\lvert \frac{\partial u}{\partial y} + \frac{\partial v}{\partial x} \right\rvert$ where $\ell_i^2 = k_1^2 y^2 D^2$, $k_1 = 0.4$, $D = 1 - \exp(-\frac{y}{A})$, $A = 26\nu_w / \sqrt{\frac{\tau_w}{\rho_w}}$ Subscript w = wall condition | Same as left hand side | Same as Rose-Balwin Baseline | $\epsilon_i = \ell_i^2 \frac{\partial u}{\partial y}$ where $\ell_i$ is the same as Rose-Balwin Baseline. | Same as Rose-Balwin Baseline | $\epsilon_i = \ell_i^2 \sqrt{\left(\frac{\partial u}{\partial y}\right)^2 + \left(\frac{\partial v}{\partial x}\right)^2}$ where $\ell_i$ is the same as Rose-Balwin Baseline | Same as Model ② | Same as Model (3) |
| Outer region | $\epsilon_o = k_2 U_{max} \delta_i^* / \gamma$ where $k_2 = 0.0168$, $\delta_i^* = \int_0^\delta (1 - \frac{u}{U_{max}}) dy$, $\gamma = 1 + 5.5 (\frac{y}{\delta})^6$ | $\epsilon_o = k_2 U_{max} \delta_i^* / \gamma$ where $k_2 = 0.0168$, $\delta_i^* = \int_0^\delta (1 - \frac{u}{U_{max}}) dy$, $\gamma = 1 + (\frac{y}{\delta})^6$ | $\epsilon_o = \ell_{max}^2 \left\lvert \frac{\partial u}{\partial y} + \frac{\partial v}{\partial x} \right\rvert$ where $\ell_{max} = 0.09\delta$ | $\epsilon_o = \ell_{max}^2 \left\lvert \frac{\partial u}{\partial y} + \frac{\partial v}{\partial x} \right\rvert$ where $\ell_{max} = 0.09\delta_o$ | $\epsilon_o = 0.0168 U_{max} \delta_i^*$ where $\delta_i^* = \int_0^\infty (1 - \frac{u}{U_{max}}) dy$ | Boundary layer: $\epsilon_o = \ell^2 \left\lvert \frac{\partial u}{\partial y} + \frac{\partial v}{\partial x} \right\rvert$ where $\ell = 0.07(\delta - y_o)$, $y_o$ = value of y at zero velocity. Wake: $\epsilon_o = 0.001176(\delta - y_o) \cdot \lvert U_\delta - U_\xi \rvert$ | $\epsilon = \frac{0.0168 U_\delta \delta_i^*}{1 + (\frac{y - y_o}{\delta})^6}$ where $\delta_i^* = \int_{y_o}^\delta (1 - \frac{u}{U_\delta}) dy$ | $\epsilon$, same as Model ② except $\delta_i^* = \int_{y_{DS}}^\delta (1 - \frac{u}{U_\delta}) dy$ where $y_{DS}$ = value of y at dividing streamline | Same as Model ③ |
| Selection | $\epsilon = Min(\epsilon_i, \epsilon_o)$ | $\epsilon = Min(\epsilon_i, \epsilon_o)$ | $\epsilon = Min(\epsilon_i, \epsilon_o)$ | $\epsilon = Min(\epsilon_i, \epsilon_o)$ | $\epsilon = Min(\epsilon_i, \epsilon_o)$ | Prescribed | Boundary layer: $\epsilon = Min(\epsilon_i, \epsilon_o)$ Separated bubble: $\epsilon = \ell_i^2 \cdot Min\left\{\left[\left(\frac{\partial u}{\partial y}\right)^2 + \left(\frac{\partial v}{\partial y}\right)^2\right]^{1/2}, \frac{U_\delta}{\gamma}\right\}$ | Separated bubble - Wall region: $\epsilon = 0.0168 U_\delta \delta_i^* \cdot \left[\frac{y}{y_{DS}}(1 - e^{-\frac{y}{A}})\right]^2$ Separated bubble - Wake region: $\epsilon = 0.0168 U_\delta \delta_i^*$ | Same as Model (3) |
| Relaxation | NO | NO | NO | $(\rho\epsilon) = (\rho\epsilon)_o + \left[(\rho\epsilon)_{eq.} - (\rho\epsilon)_o\right] \cdot \left[1 - \exp\left(-\frac{\alpha(x - x_o)}{\delta_i}\right)\right]$ if $(\rho\epsilon)_{eq} < (\rho\epsilon)_o$; $\alpha = \infty$ otherwise, $1/5$ | $\epsilon = \epsilon_{eq} + (\epsilon_o - \epsilon_{eq}) e^{-\frac{\Delta y}{\lambda}}$, $\lambda = 10\delta$, Boundary layer; $2\delta$, mixing layer | NO | NO | NO | $\epsilon(\xi) = \epsilon(\xi - \Delta\xi) + \left[\epsilon_{eq}(\xi) - \epsilon(\xi - \Delta\xi)\right] \cdot \left[1 - \exp(-\Delta\xi/\lambda)\right]$, $\lambda = 1\delta \sim 10\delta$ |

The formulation we shall adopt in the transonic flow problem is basically a hybrid relation primarily based on Rose's relaxation model and the modification suggested by Deiwert. Ingredients of the present algebraic model are blocked in heavy-lined rectangles in the preceeding table. The model for the turbulence stress $\tau_{ij}$ can be summarized as follows.

$$\tau_{ij} = \bar{\rho}\,\varepsilon \left[ \frac{\partial \bar{u}_i}{\partial x_j} + \frac{\partial \bar{u}_j}{\partial x_i} - \frac{2}{3}\frac{\partial \bar{u}_k}{\partial x_k}\delta_{ij} \right] - \frac{2}{3}\bar{\rho}\, e_s\, \delta_{ij} \qquad (1)$$

with $$\rho\, \bar{e}_s = -\frac{1}{2}\tau_{ii} \qquad (2)$$

The eddy viscosity $\varepsilon$ is estimated by the mixing length theory which subdivides the shear layer into an inner and an outer region.

<u>Inner region</u>

$$\varepsilon_I = \ell_I^{\,2}\sqrt{\left(\frac{\partial \bar{u}_i}{\partial x_j}\right)^2 + \left(\frac{\partial \bar{u}_j}{\partial x_i}\right)^2}$$

$\ell_I = k_1 y D$

$k_1 = 0.4$

$y$ = normal distance from the nearest wall

$D = 1 - \exp(-y/A)$

$A = 26\nu_w \Big/ \sqrt{|\tau_w|/\bar{\rho}}$

$\nu_w$ = kinematic viscosity coefficient at the nearest wall

$\tau_w$ = shearing stress at the nearest wall

Outer Region

$$\varepsilon_o = \ell_{max}^2 \sqrt{\left(\frac{\partial \overline{u_i}}{\partial x_j}\right)^2 + \left(\frac{\partial \overline{u_j}}{\partial x_i}\right)^2}$$

$$\ell_{max} = 0.09\delta_o$$

$\delta_o$ = boundary layer thickness

Selection $\quad \varepsilon_{eq.} = \text{Min}\ (\varepsilon_I, \varepsilon_o)$ (3)

Relaxation along a streamline-like trajectory

$$\varepsilon(\xi) = \varepsilon(\xi - \Delta\xi) + \left[\varepsilon_{eq.}(\xi) - \varepsilon(\xi - \Delta\xi)\right] \cdot \left[1 - \exp\left(-\frac{\Delta\xi}{\lambda}\right)\right] \quad (4)$$

where $\quad \lambda = \begin{cases} \infty, & \text{if } \varepsilon_{eq.} < \varepsilon(\xi - \Delta\xi) \\ 5\delta_o, & \text{otherwise} \end{cases}$

And $\xi$ is a parameter defined along a streamline.

Two major components, due to Deiwert, are introduced into Rose's formulation. One is the adoption of $\sqrt{\left(\frac{\partial \overline{u_i}}{\partial x_j}\right)^2 + \left(\frac{\partial \overline{u_j}}{\partial x_i}\right)^2}$ in place of $\left|\frac{\partial \overline{u_i}}{\partial x_j} + \frac{\partial \overline{u_j}}{\partial x_i}\right|$ to avoid the complete vanishing of $\varepsilon$ in a recirculating zone. Another one is the modification of the relaxation process in which $\varepsilon(\xi - \Delta\xi)$ is used in place of a fixed $\varepsilon$ evaluated at some reference station. Moreover, Deiwert found that relaxation over a streamline-like contour was more appropriate particularly for flows over a curved boundary, such as airfoil or turbine blade. Both modifications, indeed minor in nature, are convenient to implement with our computer code in which the scanning is done along streamline-like trajectories. The necessity of incorporating the relaxation effect has been substantiated by Baldwin and Rose (Ref. 19), Deiwert (Ref. 20), Shang and Hankey (Ref. 29). Its usefulness for flows in an unsteady transonic flow will be borne out in our forthcoming computation.



PRECEDING PAGE BLANK NOT FILMED

### 3.3 Transition to Turbulence

Laminar flow at large Reynolds numbers becomes unstable, then the growth of disturbance in the boundary layer builds up until transition to turbulence occurs. The point of transition is strongly affected by the streamwise pressure gradient and the turbulence level of the free stream. To account for these factors, several empirical methods are available (for example, van Driest and Blumer, Crabtree, Granville, Smith and Gamberoni, van Ingen, Michel). It is not possible to give a thorough comparison for those methods. In our blade-to-blade computation for flows in an impeller passage (Ref 30), both Granville (Ref 31), and Michel's (Ref 32) formulations were examined. We found that Michel's simple algorithm provided a clear-cut prediction of transition point and it was extremely easy to implement. Since boundary layer transition is such a dubious subject in numerical computation, our guideline in the selection of a criterion is again "the simpler the better." Unless future experiments contradict our selection, we shall adhere to Michel's criterion for the present application. The criterion gives a transition Reynolds number, $(Re_\theta)_{trans}$, based on the local Reynolds number $Re_x$.

$$(Re_\theta)_{trans} = 1.17\left(1 + \frac{22400}{Re_x}\right) Re_x^{0.46} \qquad (5)$$

The local $Re_\theta$ can be estimated from the incompressible momentum thickness $\theta_i$.

$$\theta_i = \int_0^\delta \frac{\bar{u}}{\bar{u}_{max}}\left(1 - \frac{\bar{u}}{\bar{u}_{max}}\right) dy \qquad (6)$$

If the local $Re_\theta$ is larger than $(Re_\theta)_{trans}$, transition to turbulent flow has taken place. Michel's criterion, resulted from correlation of experimental data, is supposingly valid for the range of $Re_x$ between $0.1 \times 10^5$ and $60 \times 10^6$. Criterion of this nature signifies that transition to turbulence occurs at a point, rather than in a region, and relaminarization is not possible. A.M.O. Smith had compared Michel's algorithm against Granville's, Smith found the simple criterion of Michel quite satisfactory in the description of transition to turbulence.

## SECTION 4

## BOUNDARY CONDITIONS FOR SIMULATION OF FREE AIR FLOW ABOUT AN AIRFOIL

This research effort concerns flow about the symmetric NACA 64A010 airfoil, which has a thickness to chord ratio of 10%, at two different angles of attack. At zero incidence the airfoil does not develop lift; hence, the circulation of the system is zero. For the 2 degrees incidence case the transonic field about this airfoil does contain circulation, since lift is being developed about the body. In this section boundary conditions are prescribed which simulate far field free air flow conditions for the non-lifting and lifting cases above.

### 4.1 Boundary Conditions for Non-Lifting Airfoil

Figure 2a shows a schematic of the domain of calculation of a symmetric airfoil having a chord C, a thickness $\tau$, and at zero degrees incidence. Let us consider inviscid, isentropic flow about this airfoil. For the case of a thin airfoil, the flow is governed by the transonic small disturbance potential equation (Ref. 4 ).

$$(1-M_\infty^2)\,\phi_{\underset{\sim}{x}\underset{\sim}{x}} + \phi_{\underset{\sim}{y}\underset{\sim}{y}} = M_\infty^2 \frac{(\gamma+1)}{U_\infty}\,\phi_{\underset{\sim}{x}}\,\phi_{\underset{\sim}{x}\underset{\sim}{x}} \tag{7}$$

where:

$$\underset{\sim}{x} = x/(C/2) \tag{8}$$

$$\underset{\sim}{y} = y/(C/2) \tag{9}$$

$$u = U_\infty + \phi_{\underset{\sim}{x}} \tag{10}$$

$$v = \phi_{\underset{\sim}{y}} \tag{11}$$

Let us define a scaled parameter $\tilde{y}$ such that

$$\tilde{y} = \delta^{\frac{1}{3}} M_\infty^{\frac{1}{2}} y \tag{12}$$

where:

$$\delta = \tau / c$$

Combination of Equations (7) and (12) yields

$$\left[K - (\gamma+1)\,\phi'_{\tilde{x}}\right]\phi'_{\tilde{x}\tilde{x}} + \phi'_{\tilde{y}\tilde{y}} = 0 \tag{13}$$

where:

$$K = (1 - M_\infty^2)/M_\infty \delta^{2/3} \tag{14}$$

$$\phi'_{\tilde{x}} = \phi_{\tilde{x}}/U_\infty \epsilon \tag{15}$$

$$\phi'_{\tilde{y}} = \phi_{\tilde{y}}/U_\infty \epsilon \tag{16}$$

$$\epsilon = \delta^{2/3}/M_\infty \tag{17}$$

Based on equations (10), (11), (15), (16), and (17), the streamwise and normal velocity components are, respectively:

$$u = U_\infty\left(1 + \epsilon\,\phi'_{\tilde{x}}\right) \tag{18}$$

$$v = U_\infty\left(\delta/M_\infty^{\frac{1}{2}}\right)\phi'_{\tilde{y}} \tag{19}$$

For the non-lifting symmetric airfoil of Figure 2a the effective far field potential solution to Equation (13) is a doublet.

$$\phi'_D = \frac{D}{2\pi\sqrt{K}}\left[\frac{\tilde{x}}{\tilde{x}^2 + K\tilde{y}^2}\right] \tag{20}$$

where D is the area of the airfoil section. Equation (20) indicates that the doublet potential strength diminishes inversely with the square of the transformed radius $\tilde{r} = (\tilde{x}^2 + K\tilde{y}^2)^{\frac{1}{2}}$ from the origin of the coordinate system, which is located at the 50 percent chord station (Figure 2a). Thus, the effects of the non-lifting airfoil on the perimeter of the system are small provided this perimeter is selected far from the airfoil.

As a result of the above, the following boundary conditions were imposed on the perimeter of the domain of calculation shown in Figure 2a.

(1) Along the upstream boundary the Murman-Cole inviscid solution (Ref. 1) is prescribed for all time.

(2) Frictionless flow is imposed along the lower horizontal lateral boundary of Figure 2a.

(3) Frictionless flow is imposed on the dividing streamline upstream and downstream of the airfoil surface.

(4) No slip flow is imposed along the airfoil surface.

(5) A two-dimensional unsteady method of characteristics, including dissipation, is employed to determine the velocity field exiting from the downstream boundary (Ref. 14).

At the upstream boundary the Murman-Cole solution is essentially the doublet of Equation (20). The lateral boundary is far enough away from the airfoil, so that any reasonable boundary condition will work including frictionless flow. Finally, at the downstream boundary the viscous equations of motion are solved, via the method of characteristics, to provide a very realistic model of the exiting flow.

## 4.2 Boundary Conditions for Lifting Airfoil

A lifting airfoil develops circulation; hence, the boundary conditions enforced on the perimeter of the system greatly influence the flow in the neighborhoo of the body. Let us consider the airfoil shown in Figure (2b) at an angle of attack $\alpha$, and having the circulation $\Gamma$. The coordinate system (x, ) is located at the 50 percent

chord station, the airfoil thickness is $\tau$, and its chord is C.

Krupp and Murman (Ref. 2) and Small (Ref. 33) have determined the far field potential solution to Equation (12) for the lifting case. The resultant equation is as follows:

$$\phi' = \phi'_D - \frac{\Gamma}{2\pi}\theta + \frac{\Gamma^2(\gamma+1)}{16\pi^2 K}\left(\frac{\ln \tilde{r}}{\tilde{r}}\right)\cos\theta - \frac{\Gamma^2(\gamma+1)}{64\pi^2 K}\frac{\cos 3\theta}{\tilde{r}} + \ldots \qquad (21)$$

where $\phi'_D$ is the doublet potential given by Equation (20) and,

$$\theta = \tan^{-1}\left(\tilde{y} K^{\frac{1}{2}}/\tilde{x}\right) \qquad (22)$$

$$\tilde{r} = \left(\tilde{x}^2 + K\tilde{y}^2\right)^{\frac{1}{2}} \qquad (23)$$

In Figure (2b) the point P is shown on the upper lateral boundary having the scaled radius $\tilde{r}$ and the angle $\theta$. The second term of Equation (21) is directly dependent on the angle $\theta$ and the circulation $\Gamma$; hence, the effects of airfoil circulation are felt throughout the domain of calculation for the lifting case. Therefore, circulation must be properly accounted for far from the body to simulate free air boundary conditions.

In order to preserve circulation throughout the domain of calculation, two sets of boundary conditions were investigated in this study. In the remainder of this section these boundary condition sets are described and their value ascertained.

In the first set of boundary conditions, the velocity field on the upstream and lateral boundaries of the system shown in Figure (2b) was calculated at each timestep from the far field small disturbance Equations (18), (19), (20), and (21). The method of characteristics, which included dissipation, was utilized to compute velocities at the downstream boundary (Ref. 14).

To obtain a more accurate velocity field on the upstream and lateral boundaries of the system, the far field small disturbance equations

(18), (19), (20), (21) were solved in conjunction with the TSFOIL (Ref. 3) inviscid field, which served as the initial conditions for the lifting calculation. The TSFOIL velocity field was used to numerically evaluate the time-independent doublet contribution to the far field potential given by Equation (21). The numerically determined doublet contribution to the far field velocities, which resulted from the initial conditions, was then saved and employed in Equation (21) at later times.

At each timestep of the calculation the lift force was computed about the airfoil and the local lift coefficient $C_L$ was determined. Based on the local lift coefficient the circulation about the airfoil, which was preserved along the perimeter of the system, was calculated from the following equation.

$$\Gamma = \frac{M_\infty^{3/4}}{\delta^{2/3}} C_L \tag{24}$$

Equation (24) is consistent with the small disturbance theory approximations.

The boundary conditions defined in this first set did not work. Vortices shed from the airfoil, whose rotation produced local velocities in the neighborhood of the upper lateral boundary (Figure (2b) ) opposite in sense to these prescribed at the lateral boundary from Equation (21). Material could not flow out of the system; therefore, the pressure built up along the upper lateral boundary eventually wiping out the wake of the airfoil.

As a result of the above, a second set of boundary conditions was prescribed in the far field. The velocity field on the upstream boundary was computed at each timestep from the far field small disturbance Equations (18), (19), (20), and (21) in a manner identical to that described above. However, along the lateral boundaries of the system (Figure 2b), far field small disturbance theory, via Equations (18), (19), (20), and (21), and the TSFOIL solution, were used

to compute only the external static pressure field along these boundaries. Based on the external far field theory pressures and the interior stresses along the lateral boundaries, the velocity field was computed from the equations of motion. Finally, the method of characteristics, described previously, was employed to compute velocities at the downstream boundary.

The boundary conditions defined in the second set worked. During the shedding process the pressure boundary condition permitted material to flow out of the system at the upper lateral boundary. This permitted the shed vortices to pass through the system and resulted in a reasonable description of the flow field for the wake of the airfoil.

## SECTION 5

## RESULTS OF NON-LIFTING CALCULATION

Computations were first conducted for the NACA 64A010 airfoil at zero degrees angle of attack. Although the Reynolds number was $4 \times 10^6$, the computations were originally made with the turbulence model turned off; a computation is now in progress with the model turned on and with a finer mesh. The laminar problem was designated "Problem 101.0"

The non-lifting airfoil numerical results for Problem 101.0 are presented in the following format:

(1) Mesh used and Initial Conditions
(2) Time-Histories of Pressure Coefficients
(3) Computational Time Reduction Factor
(4) Velocity Vectors of Steady Flow Field
(5) Surface Pressure Distribution Comparisons
(6) Mach Number Contours

### 5.1 Mesh Used and Initial Conditions

The mesh employed to solve Problem 101.0 is presented in Figure 3. This mesh is comprised of the intersection of 34 quasi-streamlines and 130 potential-like-lines. The streamline-like-line spacing is designed to provide about five points in the boundary layer downstream of the leeward airfoil shock.

The timestep levels of the mesh of Figure 3 were investigated and the speed-up factor between a multi-regional timestep run and a constant timestep run was determined. Uniform freestream conditions were assumed in the numerical investigation. The speed-up factor is the ratio of the time it would take to do a macrostep (cover the total time increment of the coarsest region) without the multi-regional timesteps to the time it would take to do the same computation with the multi-regional timesteps. Multi-regional timesteps and their speed-up factors are described in Reference 14. It was found that the minimum

timestep for the mesh of Figure 3 was 1.33 $\mu$s and the speed-up factor was 2.15. Furthermore, it was found that the potential-like-line spacing in the vicinity of the leading edge of the airfoil controlled the time-step levels.

A previous finite difference mesh was investigated, having the same number of mesh points, but with finer potential-like-line spacing in the vicinity of the airfoil leading edge. With finer potential-like-line spacing this finite difference mesh had a minimum timestep of .684 $\mu$s and a speed-up factor of 1.69. Furthermore, this mesh is still severely limited by the potential-like-line spacing in the vicinity of the airfoil leading edge, rather than the streamline-like-line spacing.

Further study is warranted to increase the speed-up factor even further by spreading potential-like-lines near the airfoil leading edge.

The initial field for the solution of Problem 101.0 was generated from the inviscid small disturbance solution from TSFOIL (Ref. 3). The initial field generated from Murman's method was interpolated onto the finite difference mesh of Figure 3 by a computer code written especially for this purpose.

A computer code, called "INTER", was developed to interpolate a flow field on a generalized finite difference mesh, termed the "unprimed points" onto another generalized finite difference mesh, termed the "primed points". The sequence of events in the interpolation process are as follows:

1. A primed point is located in the unprimed zone that contains it.
2. A first order double Taylor's series expansion is employed to interpolate the data at the four corners of the unprimed quadrilateral onto the primed point.
3. The velocity components, density, and specific internal energy are interpolated.

The INTER computer code was employed to interpolate the inviscid flow field onto the 64A010 airfoil mesh of Figure 3. The inviscid field developed by TSFOIL for the 64A010 airfoil was generated for zero angle of attack at Mach .80. The inviscid field is developed on a rectangular mesh comprised of 50 horizontal lines and 89 vertical lines and considers the airfoil as a flat plate through use of the approximate tangency condition. The airfoil mesh (see Figure 3) is comprised of 34 streamline-like-lines and 130 potential-like-lines. The interpolated pressure field on the 64A010 airfoil surface is presented in Figure 4. Measured pressure coefficients (Gross and Steinle, Ref 34) at Reynolds number $4 \times 10^6$, are also included for comparison purposes. It is seen from Figure 4 that the inviscid pressure distribution is a good approximation to these data, except in the vicinity of the shock-wave-boundary-layer interaction, and at the trailing edge of the airfoil.

## 5.2 Time-Histories of Pressure Coefficients

Starting from an initial field generated from the inviscid small disturbance solution from TSFOIL, the zero incidence case was run 1100 computational cycles to a characteristic time* $\tau$ of 3.62. The 1100 cycles required 28 minutes on the CDC 7600 computer. Pressure-time histories indicated that the field was near steady-state at this characteristic time.

In order to demonstrate that the airfoil flow field is approaching a steady-state, time histories of the pressure coefficient were monitored at five points along the surface of the airfoil. The pressure coefficient is plotted as a function of the characteristic time $\tau$ in Figure 5. It is seen from Figure 5 that at a characteristic time $\tau$

---

* Unit characteristic time corresponds to the time it takes a free stream particle to travel one chord length.

of 3.62 the time-histories are nearly horizontal. Although time-histories were not generated in other regions of the flow field, it is believed that at $\tau = 3.62$ the remainder of the field is also near steady-state.

## 5.3 Computational Time Reduction Factor

The STOKES Computer code employed to solve Problem 101.0 embodies three computational time reduction methods, namely:

1. Switched axis
2. Vector-Do-Loops
3. Multi-Regional Timesteps

It is the purpose of this section to determine the speed-up factor afforded by each method, and the total speed-up factor.

Let us consider the multi-regional timestep levels (MRT) first. Table I presents a tabulation of the timestep levels associated with the streamline-like-lines of Figure 3 at a characteristic time $\tau$ of .6600.

TABLE I

Tabulation of Timestep Levels at a Characteristic Time $\tau$ of .6606

| K-Line Range | Timestep Level | Timestep us | Number of Microsteps per Macrostep |
|---|---|---|---|
| 30-33 | 1 | .775655 | 8 |
| 25-29 | 2 | 1.55131 | 4 |
| 16-24 | 3 | 3.10262 | 2 |
| 1-15 | 4 | 6.20524 | 1 |

There are four timestep levels in Table I; hence, the computation requires eight microsteps per macrostep of computation. Each streamline-

like-line is numbered with the index K, where K=1 corresponds to the lower lateral boundary of Figure 3. It is seen from Table I that four K-lines are in Level 1, five K-lines are in Level 2, nine K-lines are in Level 3, and fifteen K-lines are in Level 4. On this basis a speed-up factor, $S_{MRT}$, can be calculated, which is the ratio of the number of point-steps that occur if the smallest timestep governs the computation to the number of point-steps that actually occur due to MRT.

$$S_{MRT} = \frac{(33)(130)(8)}{130(\ (4)(8) + (5)(4) + (9)(2) + 15)} = 3.1058 \qquad (25)$$

The speed-up factor computed above is not the maximum that could be achieved for Problem 101.0. The potential-like-lines limit the higher timestep levels. A revised mesh and a potential-line dropper in the STOKES code should give another factor of two.

The switched axes of STOKES gives a factor of 1.5 (Ref. 14) and the Vector-Do-Loops employed provides an additional factor of 1.5 (Ref. 14). Therefore, the total speed-up factor is

$$S = (1.5)\ (1.5)\ (3.1058) \approx 7.00 \qquad (26)$$

As was discussed in Section 5.2, the STOKES code was run through 1100 macrocycles to reach a near steady-state at $\tau = 3.62$. The 1100 macrocycles required 28 minutes on the Ames CDC 7600 computer. Based on Equation (26), an unswitched constant timestep version of STOKES would solve Problem 101.0 in three hours and fifteen minutes on the CDC 7600 computer.

## 5.4 Velocity Vectors of Steady Flow Field

Figures 6 and 7 present velocity vector plots of the steady flow field about the NACA 64A010 airfoil. The vectors are proportional to the particle speeds and emanate from the mesh positions of Figure 3. Figure 6 shows the leading edge flow field and the field in the

vicinity of the shock wave, while Figure 7 shows the trailing edge flow field.

A deceleration along the dividing streamline of the airfoil is shown in the flow field of Figure 6. Furthermore, subsequent expansion about the forward portion of the airfoil is also indicated in Figure 6. The boundary layer must be thin on the forward portion of the airfoil since it is not descernible in the vector plot.

Aft of the shock wave, which occurs at x=.74 ft, a thickening of the boundary layer is indicated in Figure 6. A boundary layer flow can be clearly seen at the axial station x=1.01 ft.

A recirculation region is clearly indicated in the neighborhood of the airfoil trailing edge in Figure 7. This recirculation region is only calculable through the Navier-Stokes equations; such a region is not within the scope of inviscid methods which employ a Kutta condition.

The calculated surface pressures are compared to measurements in the next section.

## 5.5 Surface Pressure Distribution Comparisons

Surface pressure distributions obtained from the STOKES numerical solution, the TSFOIL inviscid solution (Ref. 3), and the measurements of Gross and Steinle (Ref. 34) are shown in Figure 8. It is seen that the STOKES pressure distribution is nearly identical to these data, except in the vicinity of the shock and at the trailing edge. The calculated shock position, i.e., x/c = .475, appear correct; however, the shock transition is smeared out relative to these data; it is believed that the finer mesh computation now in progress will produce a sharper shock transition. The TSFOIL prediction produces a shock location aft of the experimental value, i.e., x/c = .525, but transition is sharper. Finally, at the airfoil trailing edge the TSFOIL prediction

shows an increase in pressure, while both the STOKES and experimental results indicate no such increase. The flattening of the trailing edge pressure distribution is due to viscous effects. Differences between the calculated trailing edge pressures and corresponding data may be attributed to an early numerical separation caused by the absence of turbulence. It is anticipated that the turbulent computation now in progress will greatly narrow differences between the calculated and measured pressure fields.

## 5.6 Mach Number Contours

Calculated local Mach number contours are shown in Figure 9. The freestream flow at a Mach number of .80 decelerates to a stagnation point at the leading edge of the system, then accelerates past sonic flow to Mach 1.08, shocks down to subsonic conditions, and decelerates subsonically throughout the remainder of the airfoil chord. Furthermore, a low speed recirculation region exists in the neighborhood of the trailing edge of the airfoil.

The gradual transition through the shock wave is indicated in the Mach number contours of Figure 9. The airfoil accelerates to Mach 1.08 at $x = .74$ ft, then gradually goes through shock transition to $x = .94$ ft where subsonic flow occurs. This smearing of the shock will be reduced in the finer mesh calculation now in progress.

## SECTION 6

## RESULTS OF LIFTING CALCULATION

Computations for the NACA 64A010 airfoil at two-degrees angle of attack were conducted with the turbulence and transition models operational. The turbulent lifting airfoil problem was designated "Problem 102.0". During the process of running Problem 102.0, it was found that an integrated inviscid/viscous calculation provided more realistic results than a complete viscous calculation. The principal reason for this was that the finite difference mesh employed was too coarse to define the thin boundary at the airfoil leading edge. The integrated inviscid/viscous calculation was designated as "Problem 102.1".

The lifting airfoil numerical results of Problem 102.0 are presented in the following format:

1. Finite Difference Mesh
2. Initial Conditions
3. Computational Time Reduction Factor
4. General Flow Field Structure
5. Calculated Lift and Drag

After the results of Problem 102.0 are described a discussion of Problem 102.1 follows.

### 6.1 Finite Difference Mesh

The mesh employed to solve Problem 102.0 is presented in Figure 10. This mesh is comprised of the intersection of 68 streamline-like-lines and 130 potential-like-lines. The streamline-like-line spacing is designed to provide about six points in the leeward boundary layer aft of the airfoil shock.

The mesh of Figure 10 was developed from the half-mesh employed for the NACA 64A010 airfoil at zero angle of attack (Figure 3). This half-mesh was reflected to produce a symmetric mesh about the full

64A010 airfoil at zero angle of attack. The airfoil and associated mesh were then rotated through two degrees to produce a finite difference mesh at angle of attack. Horizontal lines were then imposed at the lateral boundaries of the system and the potential-like-lines were forced to terminate at these boundaries.

In the neighborhood of the airfoil leading edge the turbulent boundary layer thickness is much smaller than the thickness of the first layer of zones adjacent to the airfoil surface. Therefore, the mesh of Figure 10 is considered as a medium mesh. It is designed to provide a practical running time with sufficient accuracy to define the important airfoil fluid mechanical phenomena.

## 6.2 Initial Conditions

The initial field for the solution of Problem 102.0 was generated from the inviscid small disturbance solution from TSFOIL (Ref. 3) for the 64A010 at $M = .8$ and 2 degrees angle of attack, and interpolated onto the mesh of Figure 10.

Initial pressure distributions on the leeward and windward sides of the airfoil are shown in Figure 11. It is seen from this figure that the leeward flow undergoes a very rapid expansion at the airfoil leading edge to supersonic flow, and then is shocked to subsonic conditions at a station along the airfoil of approximately 85% of the airfoil chord.

The inviscid lift and drag coefficients are compared to interpolated measurements of Gross and Steinle (Ref. 34) in Table II.

TABLE II

Comparison of Lift and Drag Coefficients for the NACA 64A010 Airfoil

| Method of Generation | Drag Coefficient $C_D$ | Lift Coefficient $C_L$ |
|---|---|---|
| Murman Inviscid Solution (Ref. 3 ) | .0413 | .8709 |
| Measured Value (Ref. 34) | .047 | .415 |

It is seen from Table II that the inviscid theory overestimates the lift and underestimates the drag by a large factor. If the inviscid lift prediction were closer to measurements and the flow were steady, the Murman far field solution could be imposed on the upstream and lateral boundaries of the mesh and the problem run in this way. Due to the large discrepancy in lift and the possibility of unsteady flow, the boundary conditions described in Section 4.2 were employed on these boundaries.

## 6.3 Computational Time Reduction Factor

Starting from the initial field of Section 6.2, the two degree incidence case was run 2615 macrocycles to a characteristic time $\tau$ of 9.05. The 2615 cycles required 1.88 hours on the CDC 7600 computer at Ames Research Center. Since Multi-Regional Timestep (MRT) logic is employed, each macrocycle is comprised of many microcycles. Therefore, the 1.88 hours of computational time is divided according to the timestep levels employed in the calculation. The timestep levels employed for Problem 102.0 are presented in Table III.

TABLE III

Computer Time Division

| Macrocycles | Timestep Levels | Computer Time (hrs) |
|---|---|---|
| 965 | 4 | .857 |
| 1650 | 3 | 1.023 |
| 2615 | | 1.88 |

The results of Table III indicate that the first 965 macrocycles occurred at four timestep levels, i.e., 8 microsteps per macrostep, and the remaining 1650 macrocycles occurred at three timestep levels, i.e., 4 microsteps per macrostep. Furthermore, the first 965 cycles required .857 hours of CDC 7600 time, while the remaining 1650 cycles took 1.023 hours.

Based on the results of TABLE III the speed-up factor afforded by the MRT logic can be evaluated in a manner similar to that of Section 5.3. Through the first 965 macrocycles four timestep levels were employed. The MRT speed-up factor, $S_{MRT}$, that results can be determined from Table IV below.

TABLE IV

Tabulation of Timestep Levels for First 965 Macrocycles

| Timestep Level | Layers of Zones in that Level |
|---|---|
| 1 | 12 |
| 2 | 15 |
| 3 | 28 |
| 4 | 12 |

$$S_{MRT} = \frac{(67)(13)(8)}{130(\ (12)(8) + (15)(4) + (28)(2) + 12\ )} = 2.392$$

The switched axis gives a factor of 1.5 (Ref. 13), and the Vector-Do-Loops provide another factor of 1.5 (Ref. 13); therefore, the total speed-up factor over the first 965 macrocycles is

$$S_{965} = (1.5)(1.5)(2.392) = 5.38$$

Through the remaining 1650 cycles three timestep levels were used. The MRT speed-up factor, $S_{MRT}$, can be determined from Table V below.

TABLE V

Tabulation of Timestep Levels for Remaining 1650 Macrosteps

| Timestep Level | Layers of Zones in the Level |
|---|---|
| 1 | 14 |
| 2 | 19 |
| 3 | 34 |

$$S_{MRT} = \frac{(67)(4)(130)}{130\ (\ (14)(4) + (19)(2) + 34)} = 2.0938$$

Accounting for the switched axis and Vector-Do-Loops yields a total speed-up factor of

$$S_{1650} = 4.711$$

The overall speed-up, S, is the cycle weighted average of $S_{965}$ and $S_{1650}$, i.e.,

$$S = 4.96$$

Therefore, in the absence of a switched axis code, Vector-Do-Loops, and MRT, Problem 102.0 would require 9.3 hours on the Ames CDC 7600 computer.

As was discussed previously, the timestep levels are limited by the potential-like-line spacing of the finite difference mesh in the vicinity of the airfoil leading edge, not the streamline spacing. Therefore, zone dropper logic, which drops potential-like-lines of the finite difference mesh away from the immediate neighborhood of the airfoil leading edge, would increase the number of timestep levels from four to five and decrease the number of computations required. It is believed an additional speed-up factor of two would result; hence, lifting airfoil problems could be solved within an hour.

## 6.4 General Flow Field Structure

In this section velocity vector plots are shown which illustrate the sequence of events as the viscous flow field develops from the inviscid initial conditions. Figures 12 through 17 present the velocity field of Problem 102.0 at various characteristic times ranging from zero to 8.62.

Figures 12 to 14 indicate upstream movement of the leeward airfoil shock from its initial position to its farthest upstream location. Figure 12 shows the initial inviscid field with a leeward shock clearly indicated at the 85 percent chord station. At a characteristic time $\tau$ of 2.10 (Figure 13), the leeward shock has moved to about the 40 percent chord station with a separated flow trailing the shock. In fact a clockwise vortex is seen about to shed at the trailing edge. A large clockwise vortex is shedding from the leeward side in Figure 14 ($\tau$=3.75). Furthermore, the leeward shock has moved to the 30 percent chord station, which is approximately its farthest upstream location.

Downstream motion of the shock to a near equilibrium position is indicated in the velocity vector plots of Figures 15 through 17. Figure 15 shows the velocity field at a characteristic time $\tau$ of 5.44. At this characteristic time the leeward shock is at the 35 percent

chord station. The shock has moved to approximately the 50 percent chord station at $\tau$=8.27 (Figure 16). Figure 17 at $\tau$=8.62 also indicates a leeward shock position at about the 50 percent chord station.

The main points of Figures 15 through 17 are that (a) the leeward shock seems to arrive at a near-equilibrium position, (b) vortex shedding appears to continue throughout the calculation, and (c) the wake of the airfoil assumes a sinusoidal pattern.

## 6.5 Calculated Lift and Drag

The main result of the velocity vector plots is that the flow at the airfoil trailing edge and in its wake is unsteady. To obtain a more quantitative description of this unsteadiness time-histories of the lift and drag coefficients are examined.

The lift coefficient time history is presented in Figure 18. Starting from the inviscid lift coefficient of .8709 the lift coefficient generally decreases in a transient way until a characteristic time $\tau$ of 7.6. For characteristic times greater than 7.6, the lift-time-history is periodic, with a complete period of oscillation shown in Figure 18. According to inviscid small disturbance theory (Equation 24), the circulation is proportional to lift; hence, the airfoil sheds vorticity in a transient way until $\tau$ of 7.6 and then periodic shedding occurs. From Figure 18, the period of oscillation is about 1.4 in characteristic time units.

A corresponding time history of the drag coefficient is shown in Figure 19. Starting from the inviscid drag coefficient of .0413, the drag coefficient increases to about .08 at a characteristic time $\tau$ of 3.0, then decreases to about .03 at $\tau$=6.0, and finally becomes periodic after a characteristic time of 7.6. The period of oscillation of the drag coefficient appears to be similar to that of the lift coefficient.

The lift and drag coefficients of Figure 18 and 19, respectively, are time-averaged over the period of oscillation. The time-averaged

lift coefficient $\overline{C}_L$ is .137 and the time-averaged drag coefficient $\overline{C}_D$ is .038. A comparison of these values with the corresponding interpolated measurements of Table II indicates that the calculated values are low. The calculated drag coefficient is in the ballpark, but smaller than measured, while the lift coefficient is far less than measured.

The numerical solution was examined to determine the reasons for the low lift and drag predictions. The principal reason found was that the finite difference mesh in the vicinity of the leading edge of the airfoil was too coarse to define the thin boundary layer there. The thin leading edge boundary layer is contained within the first layer of zones adjacent to the airfoil on both its leeward and windward sides. As a result the high suction pressures near the nose were not obtained numerically and the supersonic region was much smaller than that observed experimentally.

A thin leading edge boundary layer, whose thickness is smaller than the width of the first layer of zones of the finite difference mesh, has the following two numerical effects:

1. Calculated airfoil leading edge shear stresses are smaller than actual shear stresses; therefore, the predicted drag is less than the actual drag.
2. Calculated average Mach numbers in the first layer of zones about the airfoil leading edge are less than they should be. These lower Mach numbers permit the periodic flow aft of the leeward shock to erode away the expansion region on the leeside.

An alternate way of explaining the smaller calculated supersonic region is to introduce the concept of displacement thickness*. A coarse finite difference mesh at the airfoil leading edge is similar to adding a large displacement thickness to the airfoil which inhibits the leeward expansion.

---

* The authors are indebted to Dr. Gary T. Chapman of NASA Ames for suggesting this concept.

The calculated flow field contains a leeward supersonic region and a shock wave; however, the magnitude of the pressure drop due to the leeward expansion, and the shock strength are reduced below the actual expansion pressure drop and shock strength.

There are two methods of correcting this numerical problem.

1. Re-calculate the flow field with a finer mesh on the forward portion of the airfoil solving the full Navier-Stokes equations.

2. Employ another technique, which does not require a very fine mesh, to solve for the leeward supersonic region, and integrate this solution with the Navier-Stokes solution everywhere else.

It is believed that a fine mesh Navier-Stokes solution is impractical at this particular time. The finite difference mesh required is about ten times finer than what we are now using. This means that the problem will take about 20 hours to solve on the CDC 7600 computer. This computer expenditure makes Navier-Stokes computations about lifting transonic airfoils too costly for most applications.

In this research program a numerical experiment has been conducted to investigate the results of integrating another solution with the medium mesh Navier-Stokes solution of Problem 102.0. The forthcoming section describes this numerical experiment.

## 6.6 Integrated Inviscid/Viscous Calculation

The inviscid steady field from TSFOIL , employed as the initial conditions, has a much more accurate supersonic region than the medium mesh periodic Navier-Stokes solution of Problem 102.0. Furthermore, the leeward steady supersonic region computed in Problem 102.0 during the early stages of motion, i.e., at a characteristic time of 1.6, is a more accurate prediction than the TSFOIL field.

This is because the airfoil shape is properly accounted for and some viscous effects are included. The TSFOIL solution, which employs the approximate tangency condition, is interpolated to account for the body shape (see Section 5.2).

The calculated leeward supersonic field of Problem 102.0 at a characteristic time of 1.6 was integrated with the Navier-Stokes solution everywhere else in two steps.

1. At characteristic times between 7.6 and 9.05 in its period of oscillation, the periodic flow field computed in Problem 102.0 was patched together with the steady leeward supersonic region computed at $\tau$ =1.6.
2. The interface region between these solutions, which contained the leeward shock, was recomputed by running the STOKES code through a characteristic time interval of .025.

After the STOKES run, an integrated solution resulted which had a proper supersonic region, a leeward shock wave-boundary layer interaction, and a separated trailing edge region. The integrated inviscid/viscous calculation was designated as Problem 102.1.

In the remainder of this section the results of Problem 102.1 are presented. The format for presentation is as follows:

1. General Flow Field Structure
2. Calculated Lift and Drag
3. Surface Pressure Distribution Comparisons
4. Comparison of Mach Number Contours
5. Turbulence Characteristic for Airfoil

### 6.6.1 General Flow Field Structure

Shedding of vorticity from the lee side of the airfoil is indicated in the velocity vector plots shown in Figures 20, 21, 22, and 23. Figure 20 presents the velocity field at $\tau$ =7.831. A leeward vortex is forming at approximately the 50 percent chord station, while a

a vortex rotating counter-clockwise is shedding at the airfoil trailing edge. The counter-clockwise shed vortex induces clockwise circulation about the airfoil; thus, lift is enhanced. At a characteristic time of 8.204 (Figure 21), the eye of the leeward vortex of Figure 20 has moved to about the 65 percent chord station and the counter-clockwise shed vortex has moved further downstream. Figure 22, at a characteristic time of 8.649, shows the leeward vortex of Figure 21 at the airfoil trailing edge and in the process of shedding. Furthermore, the sense of this vortex is now clockwise. This shed clockwise vortex induces a counter-clockwise circulation about the airfoil; hence, the lift is reduced. At a characteristic time of 9.052, the velocity field shown in Figure 23 no longer has the clockwise leeward vortex in it; however, a counter-clockwise vortex appears to be shedding from the trailing edge. In fact, the velocity fields of Figures 20 and 23 are somewhat similar, suggesting a periodic flow.

The velocity vector plots of Figures 20 to 23 are similar to the interferogram pictures taken by Finke (Ref. 12) and shown in Figure 1. Shedding of vorticity is clearly indicated in both the interferogram pictures and velocity vector plots as well as a sinusoidal wake pattern.

Finally, the alternate shedding of counter-clockwise and clockwise rotating vortices in Problem 102.1 indicates that the instantaneous lift coefficient should fluctuate with time. Lift and drag are presented in the next section.

### 6.6.2 Calculated Lift and Drag

The periodic nature of this flow is quantitatively confirmed in calculated time-histories of the lift and drag coefficients shown in Figure 24. It is seen from Figure 24 that the instantaneous lift curve has a period of about 1.4 in characteristic time units. This period converts to a frequency of 366 hertz, or to a reduced frequency* $K$ of 4.49. The drag coefficient time history curve

* The reduced frequency $K$ is defined as the product of the angular frequency and the chord divided by the freestream velocity.

appears to exhibit the same frequency. As is shown in the velocity vector plots above, during the period of oscillation of the lift coefficient alternate shedding of counter-clockwise and clockwise vortices occur.

Independent experiments on a symmetric NACA $63_1$-012 airfoil at Mach number .70, Reynolds number $1.25 \times 10^6$, and two degrees incidence, described in Section 1, show a periodic flow at the trailing edge with a reduced frequency K of 2.5 for the oscillating shock. The discrepancy in the reduced frequency between the two cases can be attributed to differences in airfoil geometry, Reynolds number and Mach number.

The calculated instantaneous lift and drag coefficients of Figure 24 were time averaged and compared to (a) steady lift and drag measurements of Gross and Steinle (Ref. 34) and (b) lift and drag predictions of small disturbance inviscid theory (Ref. 3). The calculated time-averaged lift and drag coefficients of Problem 102.1 are compared to corresponding data in Figure 25. The predicted time-averaged lift coefficient is close to the faired experimental curve while the predicted drag coefficient is lower.

A quantitative comparison of predicted lift and drag with interpolated data of Gross and Steinle (Ref. 34), and inviscid predictions of TSFOIL are shown in Table VI.

TABLE VI

Comparison of Lift and Drag Coefficients for the NACA 64A010 Airfoil

| Method of Generation | Drag Coefficient $C_D$ | Lift Coefficient $C_L$ |
|---|---|---|
| Murman Inviscid Solution (Small Disturbance) | .0413 | .8709 |
| Measured Value (Gross and Steinle, Interpolated, TMX-62468) | .047 | .415 |
| STOKES Numerical Calculation (Problem 102.1) | .034 | .384 |

It is seen from Table VI that the calculated lift coefficient is within seven percent of the measured value, while the inviscid prediction is greater by a factor of 2.1. Furthermore, the calculated drag coefficient is somewhat lower than measured, while the inviscid prediction is closer to the data point.

The lower calculated drag coefficient is a result of the coarseness of the finite difference mesh at the leading edge of the airfoil. The leeward and windward boundary layers on the NACA 64A010 airfoil are much thinner than the thickness of the first layer of zones adjacent to the airfoil. Thus, the numerically determined shear stress at the airfoil leading edge is greatly underestimated, and results in a lower drag coefficient prediction. It is believed that for thin boundary layers at the airfoil leading edge, boundary layer theory must be integrated with Navier-Stokes computation everywhere else to produce correct drag coefficients.

### 6.6.3 Surface Pressure Distribution Comparisons

Instantaneous calculated pressure distributions on the leeward and windward sides of the NACA 64A010 airfoil are shown in Figures 26 and 27, respectively. The curves of these figures correspond to the characteristic times 7.831, 8.204, 8.649, and 9.052, which are identical to the characteristic times of the velocity vector plots of Figures 20 to 23. The leeward instantaneous pressure distributions (Figure 26) depict the periodic shedding of vortices when compared to the velocity vector plots of Figures 20 to 23.

Let us examine the leeward pressure distributions of Figure 26. Upstream of the 40 percent chord station the pressure field is steady. Curve 1, at a characteristic time of 7.831, has a high pressure point at the 50 percent chord station followed by a rarefaction whose minimum is at the 58 percent chord station. This correlates with the velocity vector plot of Figure 20 at $\tau$=7.831. Figure 20 shows a stagnation point at the 50 percent chord station followed by an expansion about the separated

region. At a characteristic time of 8.204 (Curve 2 of Figure 26), the high pressure point is at the 60 percent chord station followed by a rarefaction; this correlates with the velocity vector plot of Figure 21, which shows that the stagnation point is at the 60 percent chord station followed by an expansion about the separated region. In other words, a separated region has formed at the 50 percent chord station at $\tau$=7.831 and has moved to the 60 percent chord station at $\tau$=8.204. Curve 3 of Figure 26 ($\tau$=8.649) shows that the stagnation point has moved to the 80 percent chord station with the minimum rarefaction pressure at the 90 percent chord station. The velocity vector plot of Figure 22 ($\tau$=8.649) shows that the vortex has moved to the trailing edge of the airfoil. Finally, Curve 4 of Figure 26, at a characteristic time of 9.052, has no stagnation point followed by a rarefaction. The results of Curve 4 indicate that the vortex has shed at $\tau$=9.052.

The instantaneous windward pressure distributions of Figure 27 oscillate near the trailing edge of the airfoil. For percentage chord less than 50 percent the flow is steady on the windward side. For percentage chord greater than 50 percent oscillations are indicated. These windward trailing edge oscillations are a result of the periodic vortex shedding process that occurs on the leeward side of the airfoil.

Instantaneous calculated pressure distributions on the windward and leeward sides of the NACA 64A010 airfoil (Figures 26 and 27) were time-averaged over the period of oscillation. A comparison of the calculated time-averaged pressures with corresponding steady measurements and with predictions from inviscid small disturbance theory are presented in Figure 28. On balance the time-averaged calculated pressures compare well with corresponding data, although these data are interpolated with angle of attack. The inviscid theory predicts a shock location at the 85 percent chord station while the STOKES calculated shock location and the data indicate that the shock is at the 45 percent chord station.

### 6.6.4 Comparison of Mach Number Contours

Mach number contours about the NACA 64A010 airfoil are compared in Figures 29 and 30. Figure 29 presents the TSFOIL inviscid solution, while Figure 30 represents the STOKES prediction at a characteristic time of 8.65. The most striking differences between the two figures are the extent of the leeward supersonic region and the locus of the leeward shock. The inviscid flow field expands about the leeward side of the airfoil to a supersonic Mach number of 1.3 and then goes through shock transition at the 85 percent chord station. In contrast, the viscous field at $\tau$=8.65 has a supersonic expansion to Mach 1.2 and goes through shock transition at about the 45 percent chord station.

The results of Figures 29 and 30 are similar with respect to the thickness of the shock transition region. Both fields have a leeward shock layer approximately 5 percent of a chord thick. The finite shock layer of Figure 30 is a result of the STOKES numerical method and the finite difference mesh employed in the shock region. If shock fitting is not employed, shock transition usually takes place across four zones of the finite difference mesh. Hence, the spacing of these four zones defines the thickness of the shock layer. In this particular case the layer is approximately 5 percent of a chord thick. A finer mesh in the shock region can reduce the thickness of this layer.

The viscous wake of the airfoil is also indicated in Figure 30. In fact, at a station x of about 2.80 the eye of a vortex can be seen in the Mach number contour plot. At approximately this station a closed

Mach .80 contour contains a closed Mach .90 contour, indicating a decrease in velocity as one moves away from the eye of the vortex.

Finally, it is pointed out that the Mach number contour plot of Figure 30 represents a snapshot of the field at a characteristic time of 8.65. The leeward shock actually oscillates and vortex shedding occurs. From an examination of the instantaneous leeward pressure distributions of Figure 26, it is seen that the amplitude of the oscillation is small, i.e., about one percent of a chord. This is consistent with the data of Finke (Ref. 12 and Section 1) for the NACA $63_1$-012 airfoil at Mach .70 and Reynolds number $1.25 \times 10^6$. Finke found that the shock amplitude was about one percent of a chord for $\alpha = 2^\circ$ and increased to 18% of a chord at $\alpha = 8^\circ$. Thus, as the angle of attack is reduced towards zero the leeward shock approaches an equilibrium position and steady flow is achieved.

### 6.6.5 Turbulence Characteristics for Airfoil

Due to the transient nature of the flow aft of the leeward shock wave, it is difficult to assess the validity of the Rose turbulence model employed in this numerical investigation. However, numerically determined eddy viscosity profiles upstream and downstream of the leeward shock qualitatively compared with corresponding profiles on a flat plate undergoing a shock-wave boundary layer interaction.

Profiles of the ratio of the eddy viscosity $\epsilon$ to the molecular viscosity $\mu$ are presented in Figure 31 at two chord stations along the leeward side of the NACA 64A010 airfoil. These data correspond to a characteristic time $\tau$ of 8.65. The profile on the left hand side of the figure, which is at the 31.4 percent chord station, is upstream of the shock, while the profile on the right hand side of the figure, which is at the 61.1 percent chord station, is downstream of the shock. Upstream of the shock the $\epsilon/\mu$ profile is nearly linear through the laminar sublayer and a portion of the turbulent boundary

layer, constant through the remainder of the boundary layer and then rapidly decays as the local freestream is approached. Downstream of the leeward shock the velocity profile is separated in the vicinity of the wall. The separated velocity profile causes the eddy viscosity to approach zero near the wall and results in a nearly linear $\epsilon/\mu$ profile in the shear layer above the wall. The linear $\epsilon/\mu$ region is followed by a constant value throughout the remainder of the boundary layer and then a rapid decay to local freestream conditions. A comparison of the calculated $\epsilon/\mu$ profiles upstream and downstream of the shock indicates that the turbulence intensity increases through the shock transition.

The qualitative behavior of the calculated STOKES $\epsilon/\mu$ profiles is similar to corresponding $\epsilon$ profiles calculated by Baldwin and Rose (Ref. 19) on a flat plate. Baldwin and Rose used a relaxation eddy coefficient model to investigate a shock wave-boundary layer interaction on a flat plate at Mach 2.39 and Reynolds number per meter of $5.7 \times 10^7$. The Baldwin and Rose profiles upstream of and downstream of the shock are presented in the upper right corner of Figure 31. It is seen from Figure 31 that the Baldwin and Rose $\epsilon$ profiles upstream of and downstream of the flat plate shock are similar in shape to corresponding NACA 64A010 $\epsilon/\mu$ profiles upstream of and downstream of the leeward shock.

## SECTION 7

## CONCLUSIONS AND RECOMMENDATION

The present investigation has demonstrated that the STOKES computer code is an accurate, practical tool for solving viscous, compressible lifting and non-lifting airfoil problems at transonic Mach numbers and for Reynolds numbers ranging from the laminar to turbulent regimes. Applicability to the turbulent Reynolds number regime was achieved by employing the Baldwin-Rose mixing length theory to which relaxation along a streamline-like trajectory is incorporated.

The numerical method embodied in the STOKES code offers a complete, accurate description of the viscous flow field about a transonic airfoil, including the important fluid mechanical effects of

1. shock wave-boundary layer interactions,
2. transonic buffet and
3. circulation for the lifting case.

Furthermore, a Kutta condition, whose formulation for unsteady flow is quite uncertain, is not required in this method.

Accuracy of the numerical method was demonstrated in numerical-experimental comparisons for two transonic airfoil cases. The three fluid mechanical effects defined above were computed and verified experimentally. At zero degrees angle of attack a shock wave-boundary layer interaction was successfully computed and verified for the NACA 64A010 airfoil. At two degrees incidence periodic motion (transonic buffet) was calculated along the aft portion of the airfoil and in its wake; this periodic motion has been observed for other airfoil geometries at transonic speeds. Although no measurements for the unsteadiness of the flow field were made for the NACA 64A010 airfoil at these conditions, steady measurements of lift, drag and surface static pressures compared favorably with corresponding computed time-averaged lift, drag, and surface static pressures. Finally, at two degrees incidence the flow field was computed with far field boundary

conditions that simulated the free air case and preserved the airfoil circulation throughout the flow field.

Practicality of the STOKES computer code was demonstrated by the Ames CDC 7600 computer time requirements for the two cases solved. For the non-lifting case the steady flow field was computed in 28 minutes, while for the lifting case the periodic flow field was computed in 1.88 hours.

The major criticism of the present method of solution is perhaps the accuracy with which the shear stresses are computed at the leading edge of the airfoil. Due to the coarseness of the leading edge finite difference mesh relative to the boundary layer thickness there, the calculated leading edge shear stress distribution and hence, the drag, was lower than measured. Therefore, it is recommended that in the neighborhood of the airfoil leading edge, boundary layer theory be integrated with Navier-Stokes computation everywhere else. This will produce correct drag coefficients with a minor increase in computational time.

## SECTION 8

## REFERENCES


1. Murman, E. M. and Cole, J. D., "Calculation of Plane Steady Transonic Flows," AIAA Journal, Vol. 9, No. 1, pp 114-121, January, 1971.

2. Krupp, J. A. and Murman, E. M., "Computation of Transonic Flow Past Lifting Airfoils and Slender Bodies," AIAA Journal, Vol. 10, No. 7, pp. 880-886, July 1972.

3. E. M. Murman, F. R. Bailey, and M. L. Johnson: "TSFOIL --A Computer Code for Two-Dimensional Transonic Calculations, Including Wind-Tunnel Wall Effects and Wave-Drag Evaluation", NASA SP-347, Part II, Aerodynamic Analyses Requiring Advanced Computers, pp. 769-788, 1975.

4. Liepmann, H. W. and Roshko, A., Elements of Gas Dynamics, p. 205, Wiley, New York, 1957.

5. Ibid, p. 204.

6. Bower, F., Garabedian, P., Korn, D., and Jameson, A., Lecture Notes in Economics and Mathematical Systems, Supercritical Wing Section II, Vol. 108, Springer-Verlog, 1973.

7. Magnus, R. and Yoshihara, H. "Inviscid Transonic Flow Over Airfoils," AIAA Journal, Vol. 10, 12, pp. 2157-2162, December 1970.

8. Murphy, J. D. and Davies, C. B.,"Users Guide - AMES INLET Boundary Layer Program MK I," NASA TMX-62-211, January 1973.

9. Murphy, J. D., Presley, L. L., and Rose, W. C., "On the Calculation of Supersonic Separating and Reattaching Flow," AGARD Proceeding Paper 23, May 27-30, 1975. Gottingen, Germany.

10. Reference 3, p. 270.

11. McDevitt, J. B., Levy, L. L., and Deiwert, G. S., "Transonic Flow About a Thick Circular-Arc Airfoil," AIAA Journal, Vol. 14, No. 5, pp. 606-613, May 1976.

12. Finke, K., "Unsteady Shock Wave-Boundary Layer Interaction on Profiles in Transonic Flow," AGARD Conference Proceedings No. 168, AGARD-CP-168, FLOW SEPARATION, Fluid Dynamics Panel Sympoisum, Gottingen, Germany 27-30 May 1975.

13. Trulio, J. G., "Theory and Structure of the AFTON Codes," Air Force Weapons Laboratory Technical Report No. AFWL-TR-66-19, 1966.

14. King, L. S., Walitt, L., Enos, J., "An Investigation of Computational Time Reduction Methods for Solving the Navier-Stokes Equations," NASA TMX-73, 102, October 1975.

15. Magnus, R. J. and Yoshihara, H., "Calculations of Transonic Flow Over an Oscillating Airfoil," AIAA Paper 75-98, AIAA 13 Aerospace Sciences Meeting, Pasadena, CA, January 20-22, 1975.

16. Trulio, J. G. and Walitt, L., "Numerical Calculation of Viscous Compressible Flow Around an Oscillating Rigid Cylinder," NASA CR-1967, 1969.

17. Trulio, J. G., Carr, W. E., Germroth, J. J., and McKay, M. W., "Numerical Ground Motion Studies, Volume III, Ground Motion Studies and AFTON Development," Air Force Weapons Laboratory Report No. AFWL TR-67-27, 1969.

18. King, L. S., Walitt, L., and Enos, J., "An Investigation of Computational Time Reduction Methods for Solving the Navier-Stokes Equations," NASA TN to be published.

19. Baldwin, B. S., and Rose, W. C., "Calculation of Shock-Separated Turbulent Boundary Layers," Proceedings NASA Conference on Aerodynamic Analyses Requiring Advanced Computers, Langley, Virginia, March 1975, NASA SP-347, Part I, pp. 401-418.

20. Deiwert, G. S., "Computation of Separated Transonic Turbulent Flows," Private Communication. See also Deiwert, G. S., McDevitt, J. B., and Levy, L. L., Jr., "Simulation of Turbulent Transonic Separated Flow," Proceedings NASA Conference on Aerodynamic Analyses Requiring Advanced Computers, Langley, VA. March 1975, NASA SP-347, Part I, pp. 419, 436.

21. Baldwin, B. S., and MacCormack, R. W., "Numerical Solution of the Interaction of a Strong Shock Wave with a Hypersonic Turbulent Goundary Layer," AIAA Paper 74-558, AIAA 7th Fluid and Plasma Dynamics Conference, June 1974.

22. Cebeci, T., "Calculation of Compressible Turbulent Boundary Layers with Heat and Mass Transfer", AIAA Journal, Vol. 9, No. 6, p. 1091, 1971.

23. Cebeci, T., Smith, A. M. O. and Mosinskis, G., "Calculations of Compressible Adiabatic Turbulent Boundary Layers," AIAA Journal, Vol. 8, No. 11, p. 1974, 1970.

24. Kolmogorov, A. N., "Equations of Turbulent Motion of an Incompressible Liquid," Izv. Akad. Nauk SSR Seria fizichiska VI, No. 1-2, p. 56, 1942.

25. Saffman, P. G., "A Model for Inhomogeneous Turbulent Flow, Proc. Roy. Soc., A317, p. 417, 1970.

26. Wilcox, D. C., "Calculation of Turbulent Boundary-Layer Shock-Wave Interaction," AIAA Journal Vol. II, No. 11, p. 1592, 1973.

27. Prandtl, L., "Bericht uber Untersuchungen zur ausgebildeten Turbulenz," ZAMM, Vol. 5, p. 136, 1925.

28. Van Driest, E. R., "On Turbulent Flow Near a Wall," J. Aerospace Sci., Vol. 23, No. 11, p. 1007, 1956.

29. Shang, J. S. and Hankey, W. L., Jr., "Numerical Solution of the Navier-Stokes Equations for Supersonic Turbulent Flow over a Compression Corner," AIAA Paper 75-4, 1975.

30. Walitt, L., Harp, J. L., Jr., and Liu, C. Y., "Numerical Calculation of the Internal Flow Field in a Centrifugal Compressor Impeller", NASA CR-134984, Dec. 1975.

31. Granville, P. S., "The Calculation of the Viscous Drag of Bodies of Revolution," Rep. 849, David Taylor Basin, 1953.

32. Michel, R., "Étude de la Transition sur les Profiles d'aile; Establissement d'un Critere de Determination due Point de Transition et Calculde la Trainee de Profile Incompressible," O.N.E.R.A. Report 1/1578A, July 1951.

33. Small, R. D., TAE Report 273, Technian, Israel, February 1976.

34. Gross, A. R. and Steinle, F. W. "Pressure Data from 64A010 Airfoil at Transonic Speeds in Heavy Gas Media of Ratios of Specific Heats from 1.67 to 1.12", NASA TMX-62-468, August 1975.

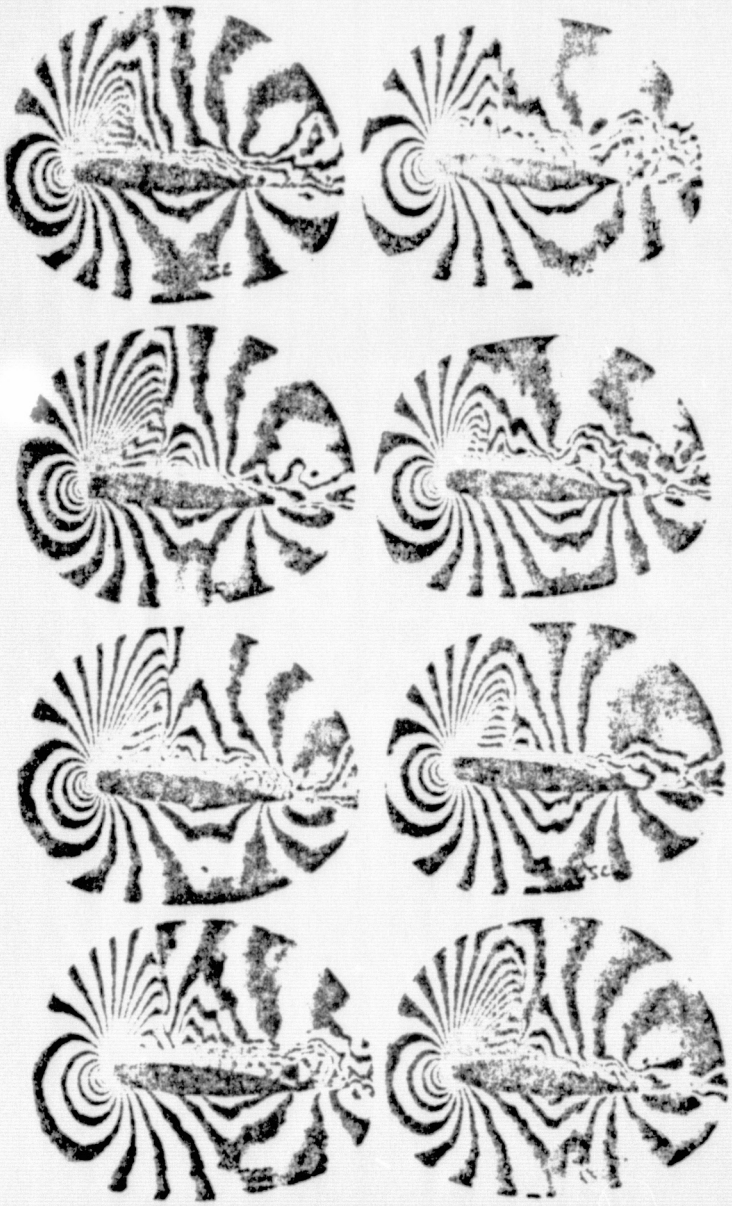

Figure 1. Interferogram pictures of the time-dependent flow field over the NRL 0.1025-0.6750-1.300 airfoil at M =.71, $\alpha = 5^\circ$, and $Re_{c_\infty} = 1 \times 10^6$; pictures depict one full period of leeward shock oscillation at intervals of 700 microseconds.

PRECEDING PAGE BLANK NOT FILMED

(a) Non-Lifting Symmetric Airfoil

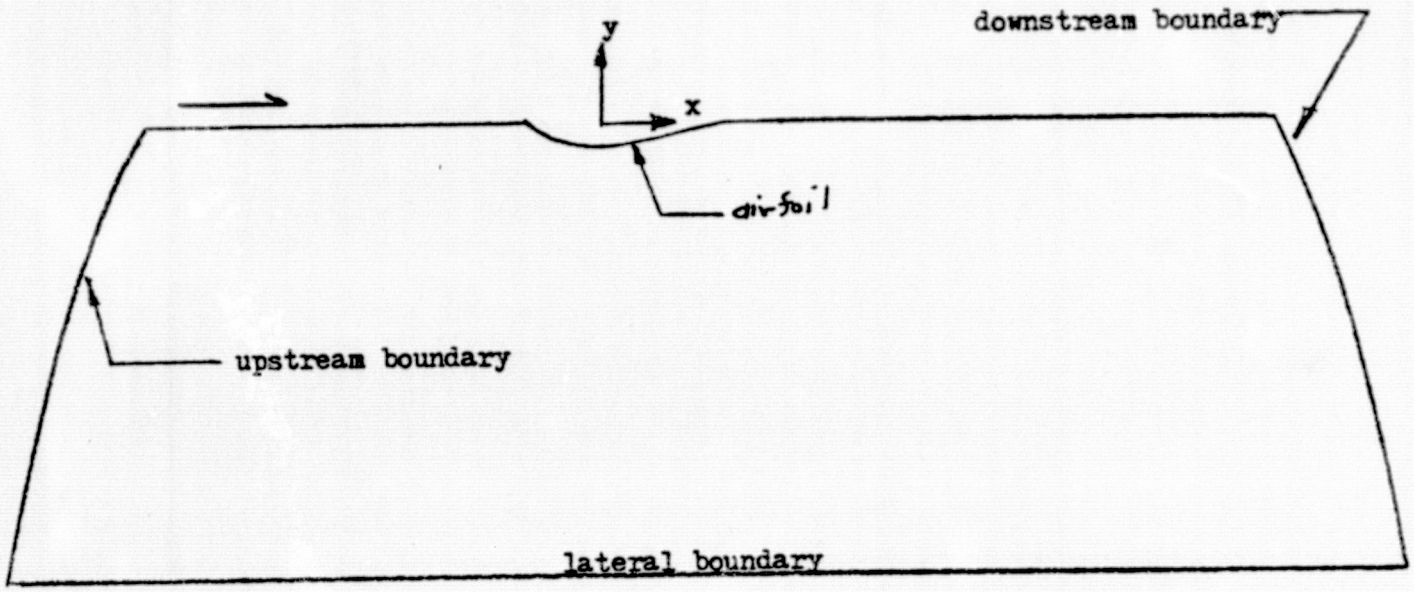


(b) Lifting Symmetric Airfoil

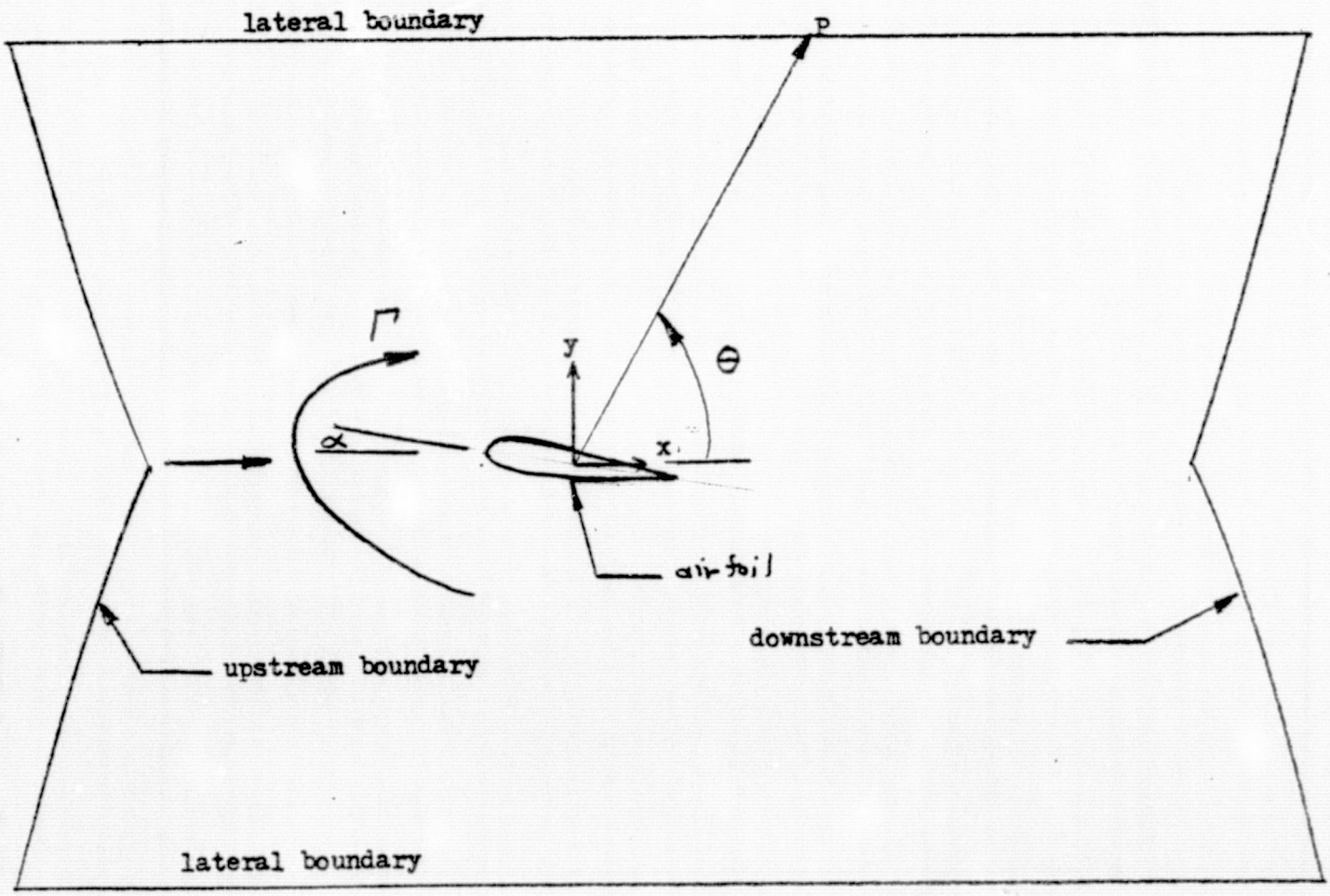


Figure 2. Schematic of far field boundary conditions for lifting and non-lifting airfoils.

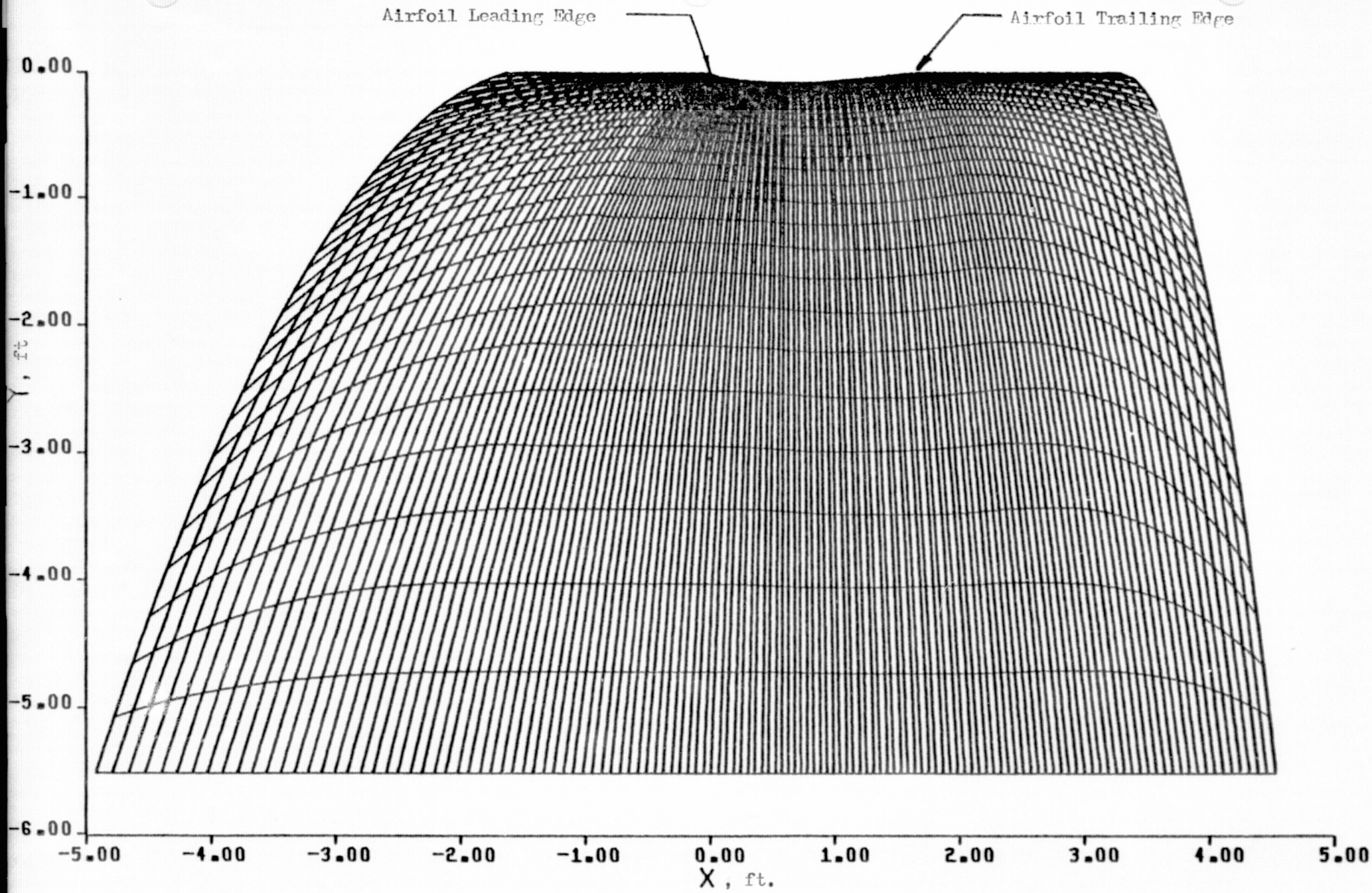


Figure 3. Finite difference mesh for 64A010 airfoil computation; mesh comprised of 34 streamline-like-lines and 130 potential-like-lines.

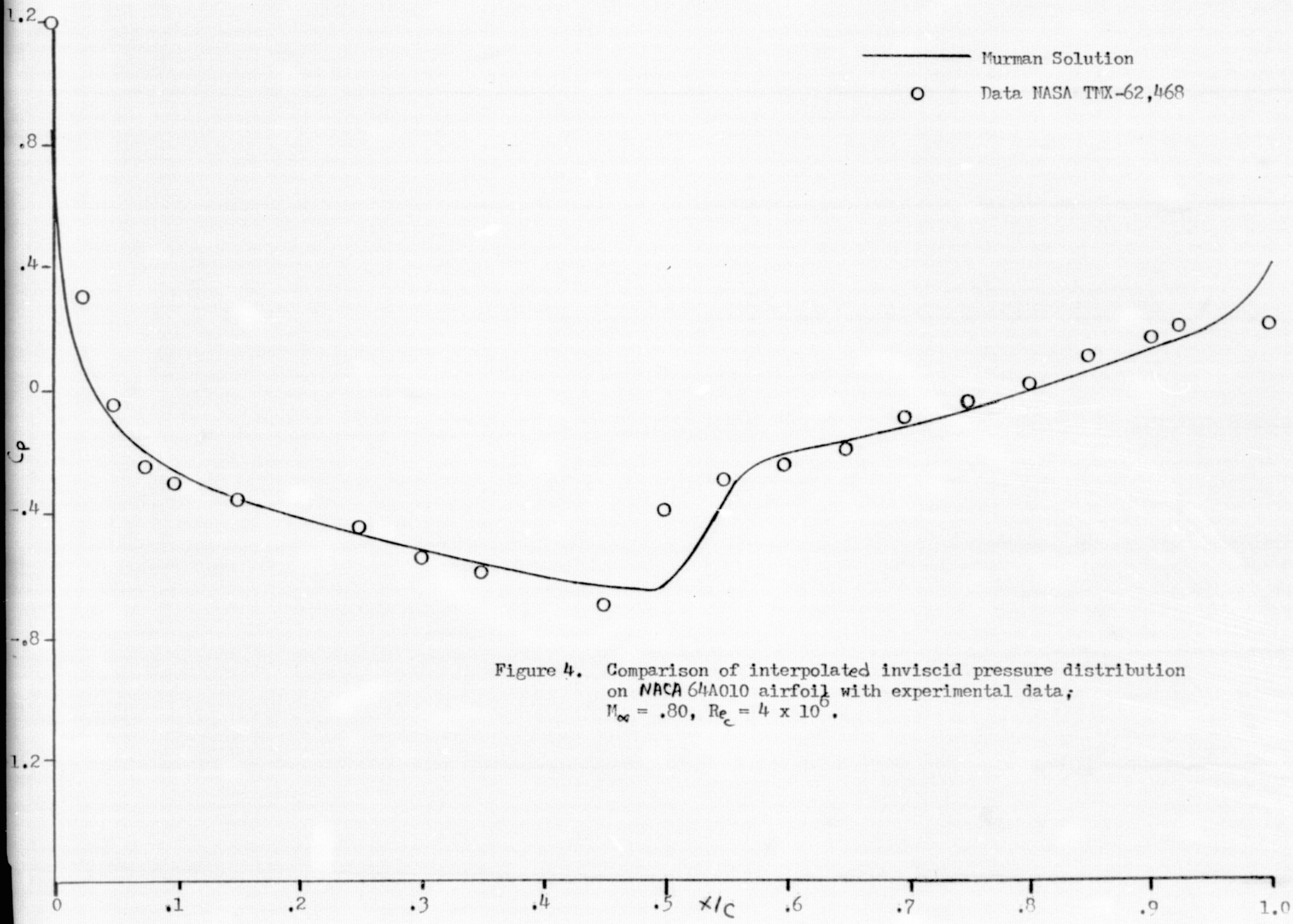


Figure 4. Comparison of interpolated inviscid pressure distribution on NACA 64A010 airfoil with experimental data; $M_\infty = .80$, $Re_c = 4 \times 10^6$.

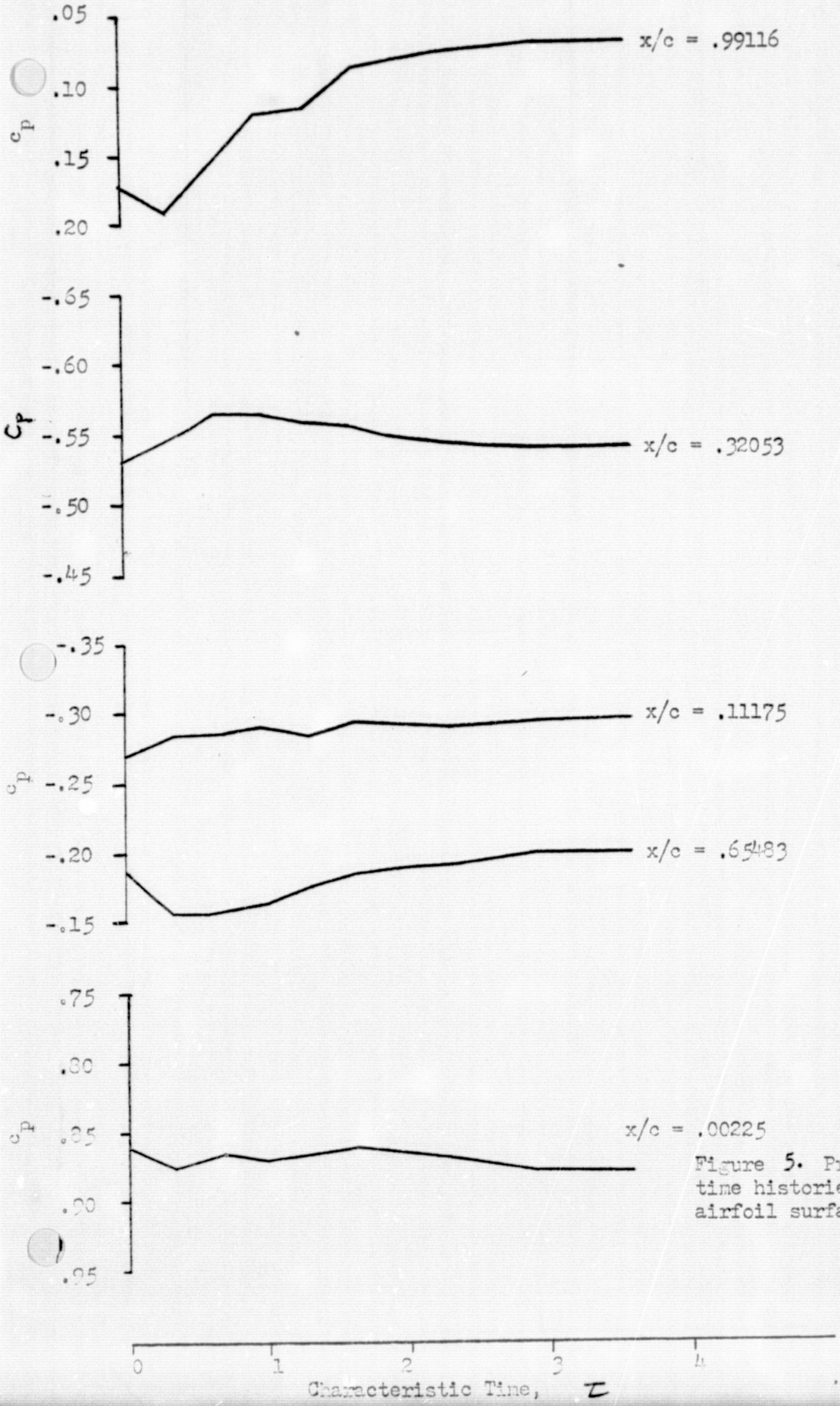


Figure 5. Pressure coefficient time histories on NACA 64A010 airfoil surface.

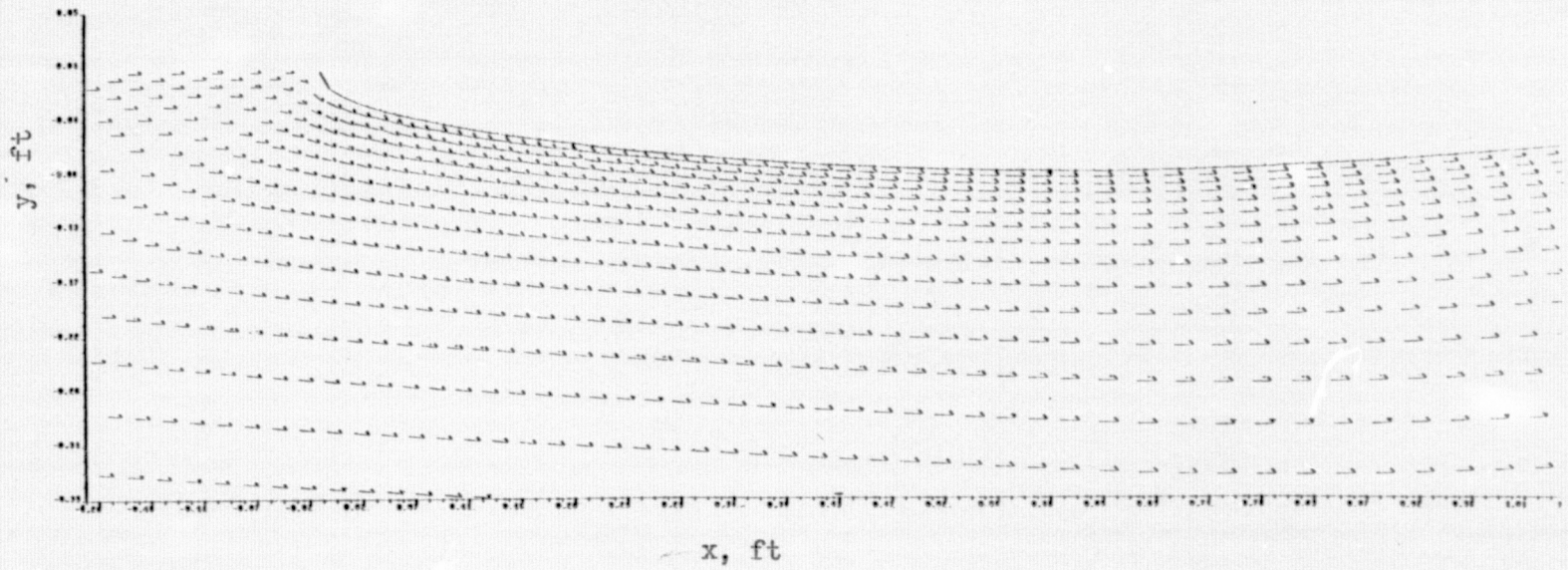


Figure 6. Velocity vector plot of the flow field on the forward portion of the NACA 64A010 airfoil; $M_\infty$=.80, $Re_{\infty_c}$ =4 x $10^6$, $\alpha$ =0.

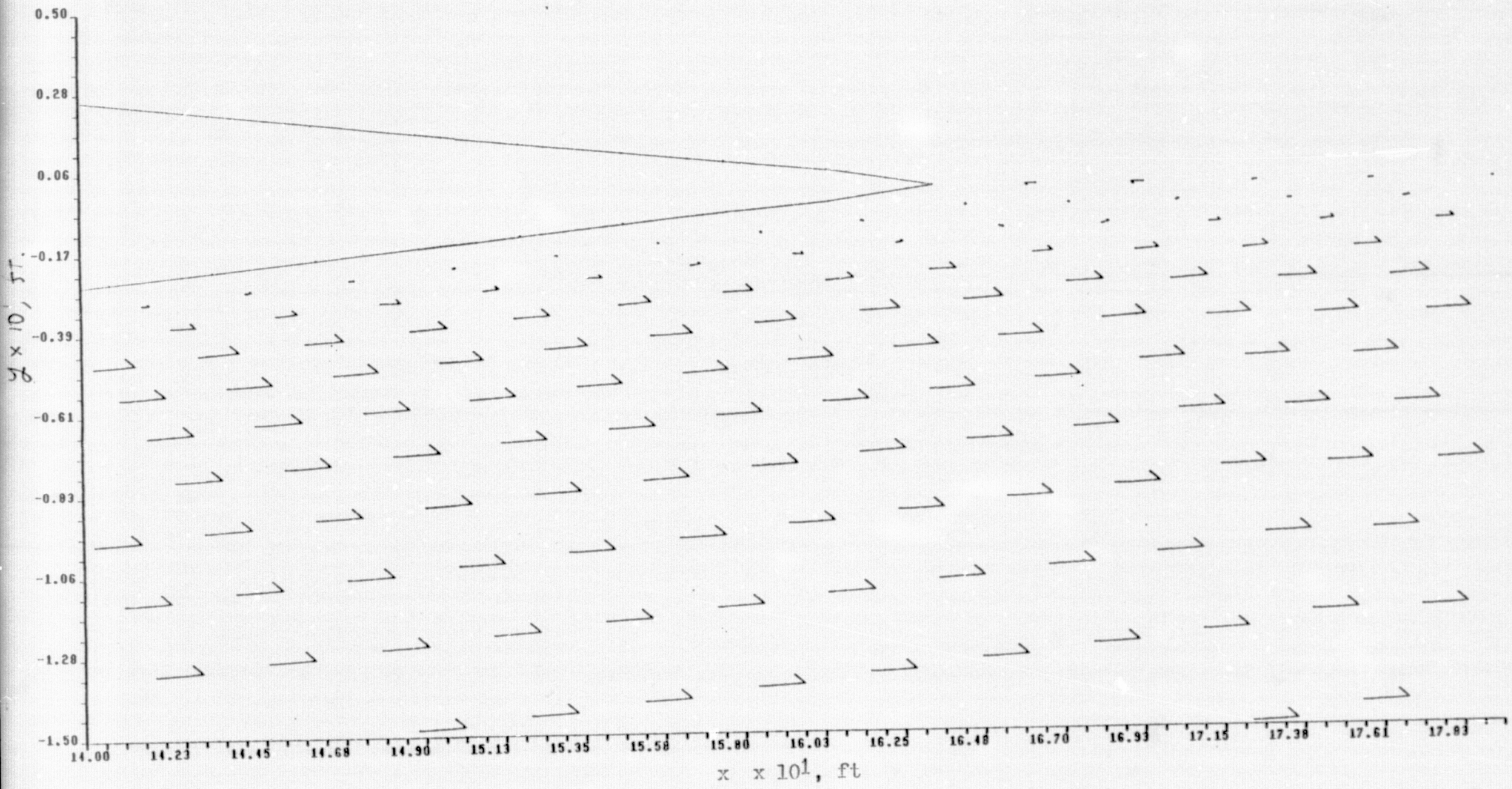


Figure 7. Velocity vector plot of the trailing edge flow field of the 64A010 airfoil; $M_\infty = .80$, $Re_\infty = 4 \times 10^6$, $\alpha = 0^\circ$.

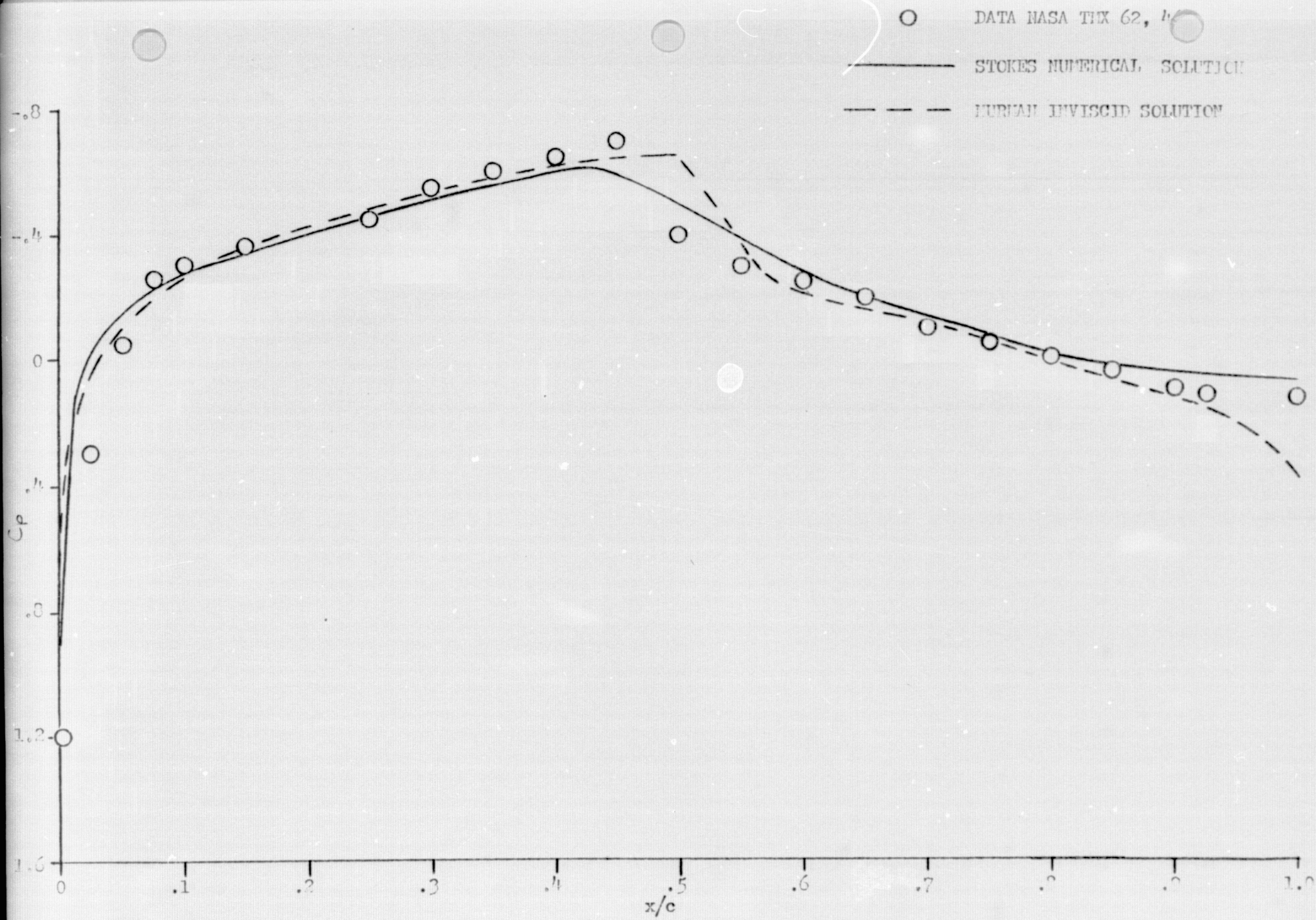


Figure 8. Comparison of numerical, inviscid, and experimentally determined pressure distributions on the NACA 64A010 Airfoil; $M_\infty$=.80, $R_{e_c}$=x $10^6$, $\alpha$=0.

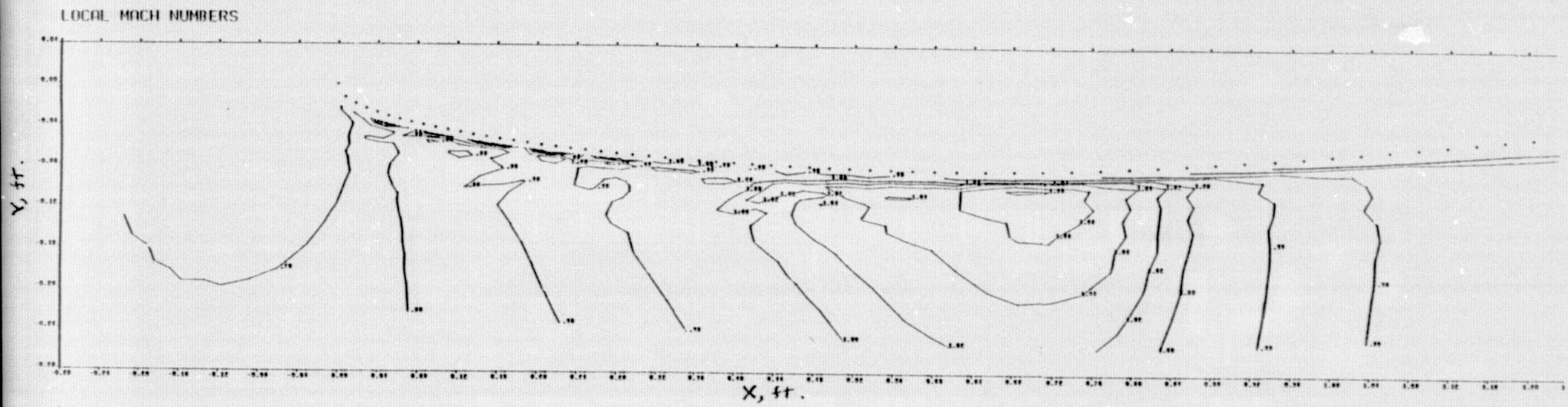


Figure 9. Local Mach number contours about the NACA 64A010 airfoil at zero incidence; $M_\infty = .80$, $Re_{c_\infty} = 4 \times 10^6$.

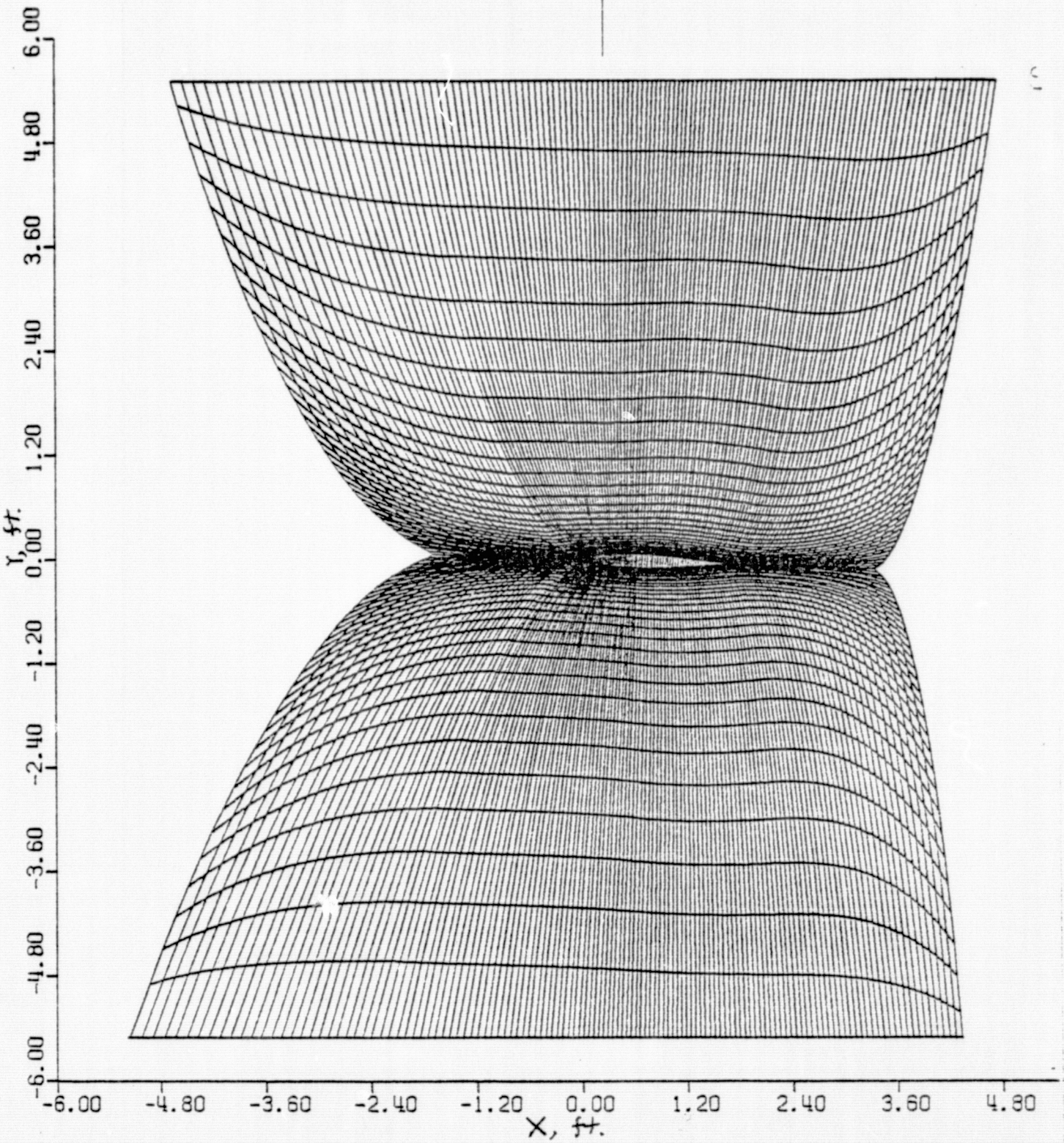


Figure 10. Medium finite difference mesh for NACA 64A010 airfoil at two degrees angle of attack, Problem 102.0 - mesh comprised of 68 streamlike-lines and 130 potential-like-lines.

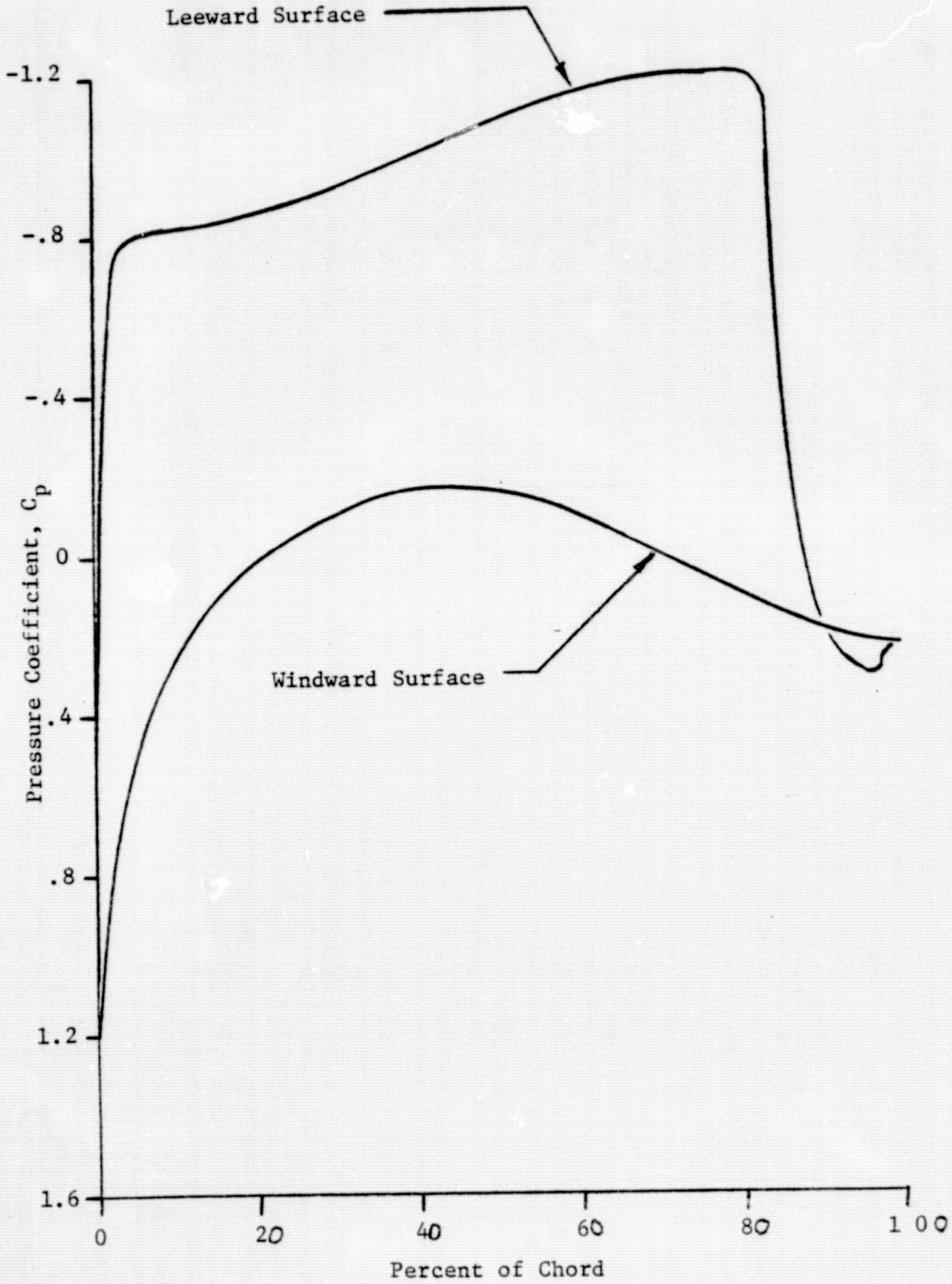


Figure 11. Initial pressure distributions on the leeward and windward surfaces of the NACA 64A010 airfoil; $M_\infty$=.8, $\alpha=2^0$, $Re_{\infty c}$= 4 x $10^6$.

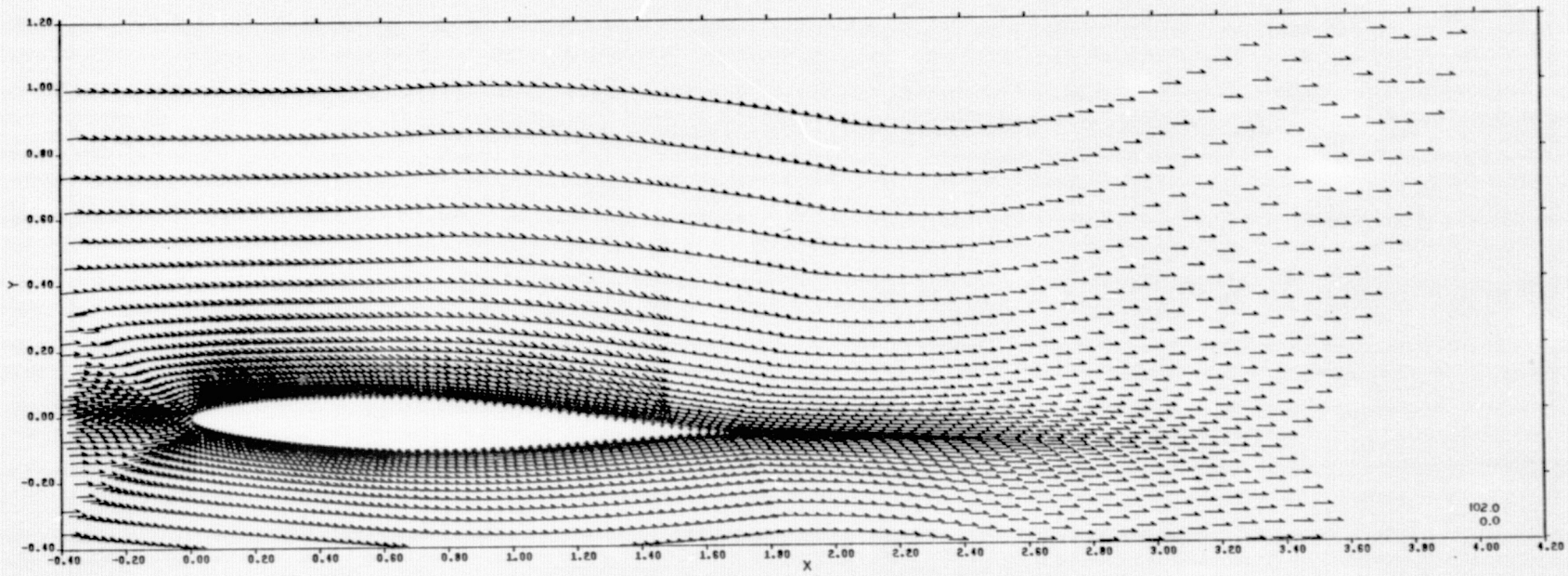


**Figure 12. Velocity vector plot of the initial flow field about the NACA 64A010 airfoil; $M_\infty = .80$, $Re_{c_\infty} = 4 \times 10^6$; Problem 102.0**

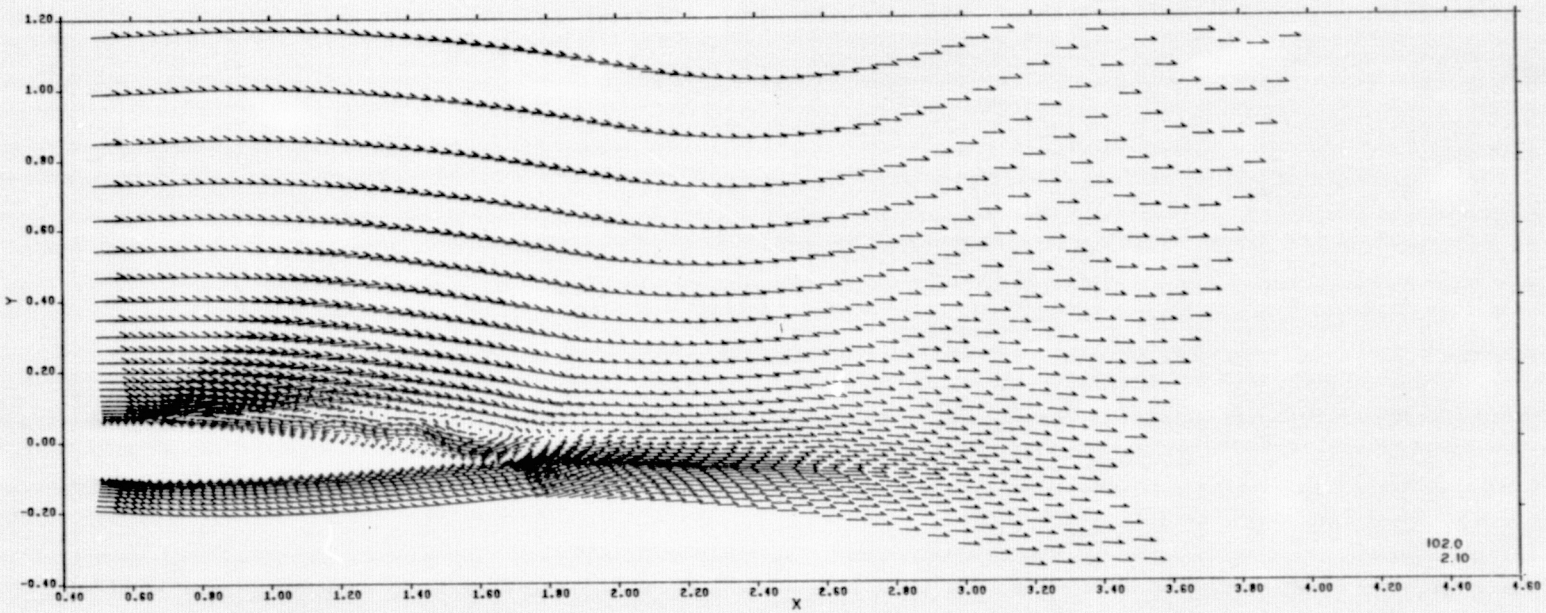


Figure 13. Velocity vector plot of the NACA 64A010 airfoil flow field at a characteristic time of 2.10; $M_\infty = .80$; $\alpha = 2°$; $Re_{c_\infty} = 4 \times 10^6$; Problem 102.0

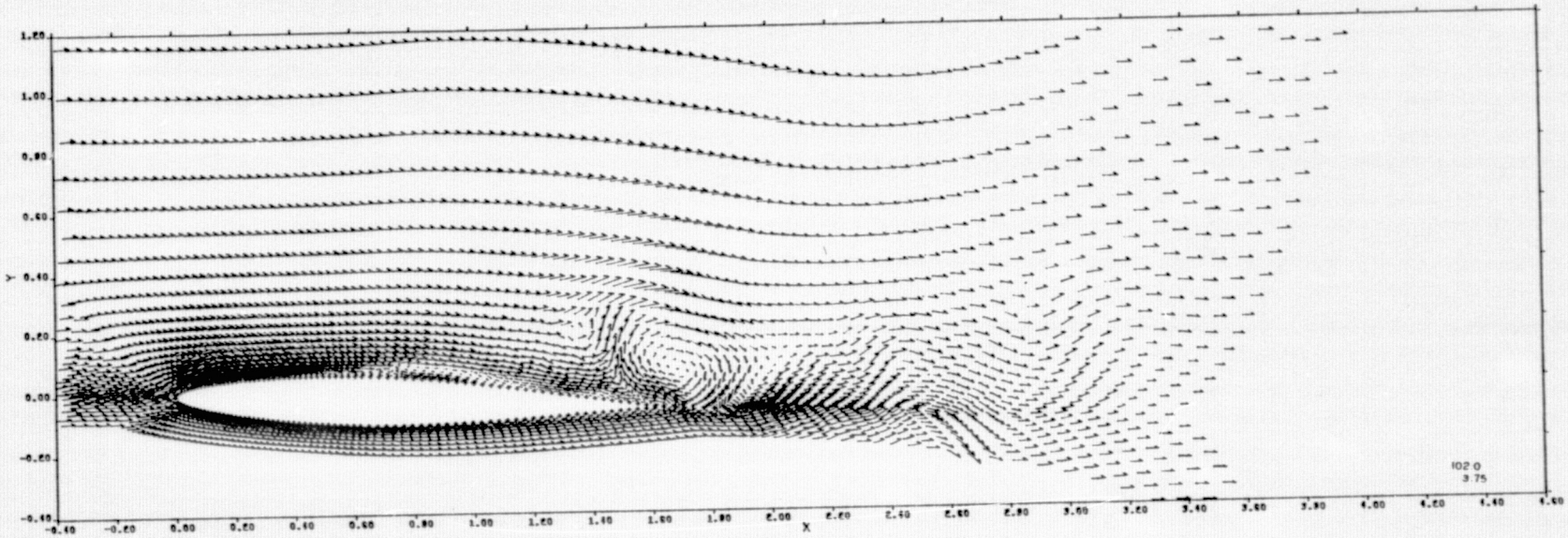


Figure 14. Velocity vector plot of the NACA 64A010 airfoil flow field at a characteristic time of 3.75; $M_\infty = .80$; $\alpha = 2^\circ$; $Re_{c_\infty} = 4 \times 10^6$; Problem 102.0

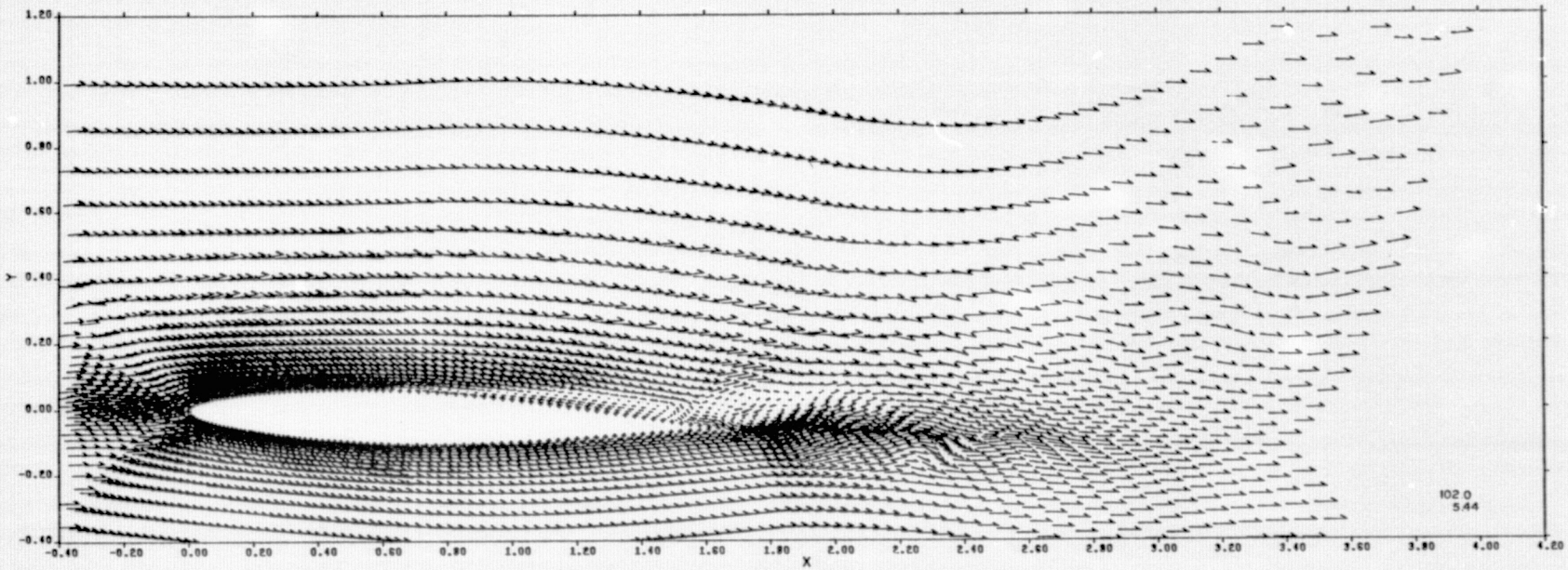


Figure 15. Velocity vector plot of the NACA 64A010 airfoil flow field at a characteristic time of 5.44; $M_\infty = .80$; $\alpha = 2°$; $Re_{c_\infty} = 4 \times 10^6$; Problem 102.0.

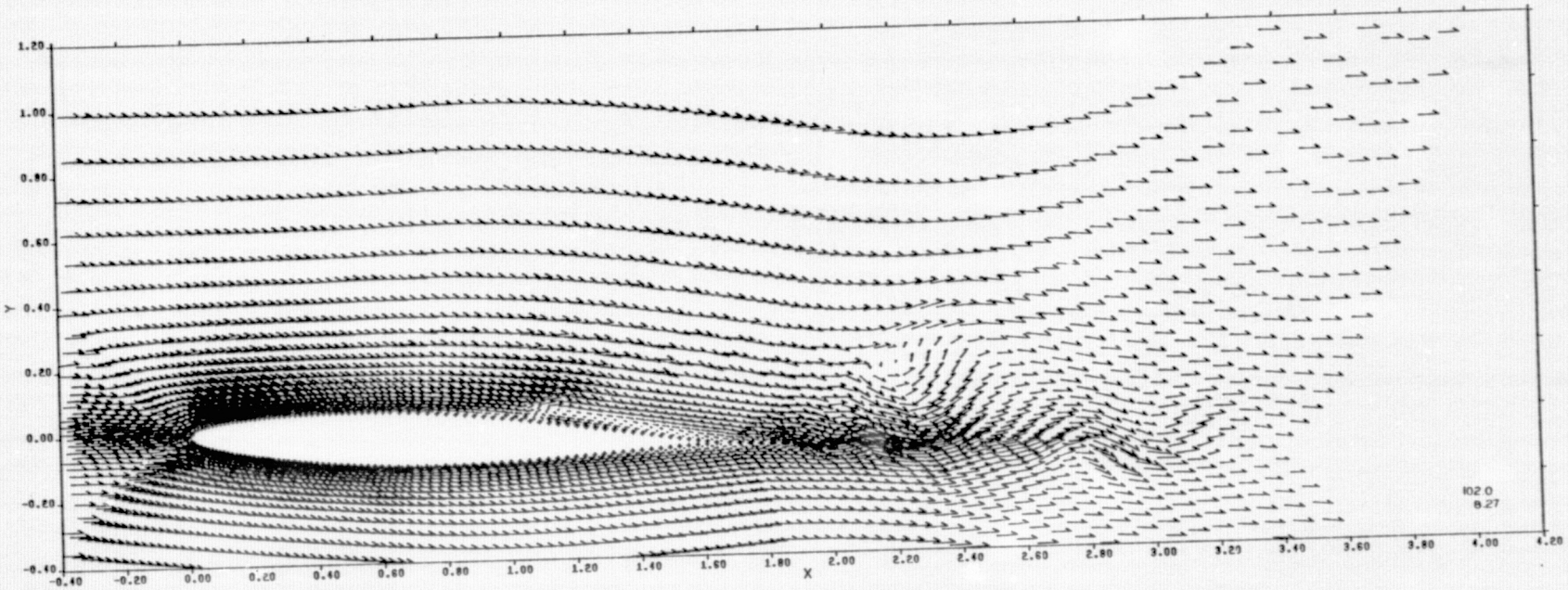


Figure 16. Velocity vector plot of the NACA 64A010 airfoil flow field at a characteristic time of 8.27; $\alpha = 2^{\circ}$; $Re_{c_\infty} = 4 \times 10^6$; Problem 102.0.

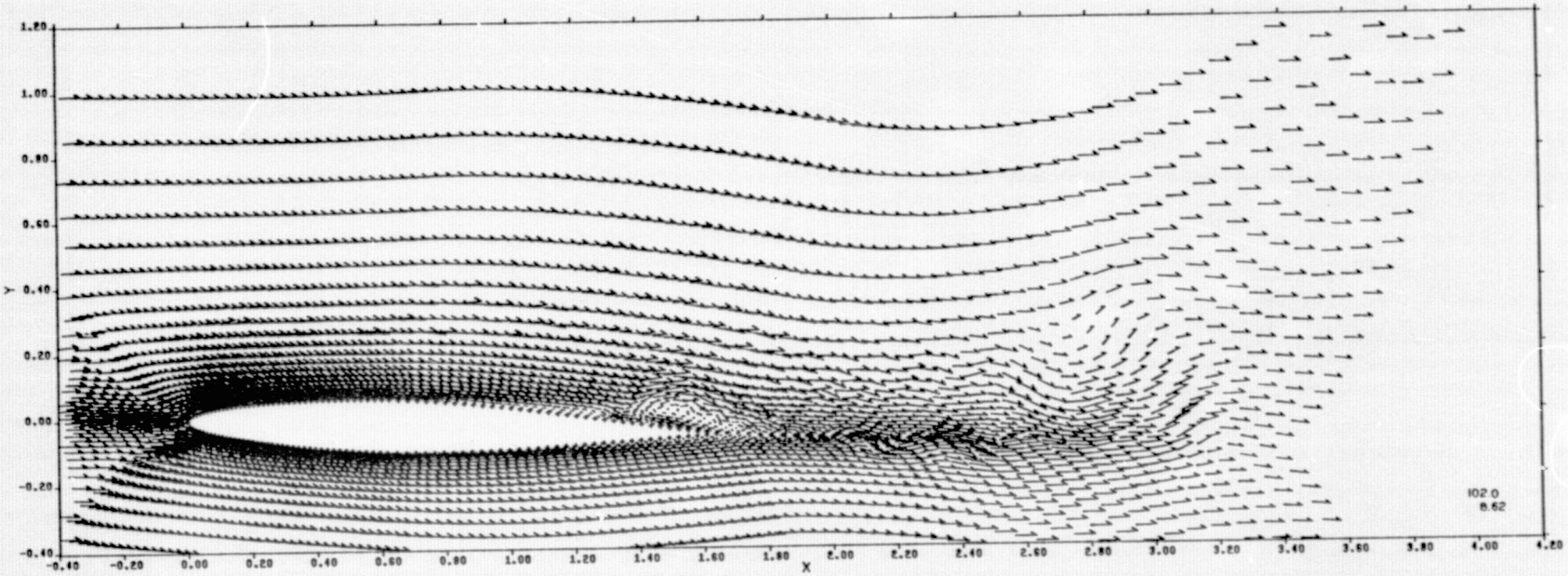


Figure 17. Velocity vector plot of the NACA 64A010 airfoil flow field at a characteristic time of 8.62, $\alpha = 2^\circ$; $Re_{c_{\infty}} = 4 \times 10^6$; Problem 102.0.

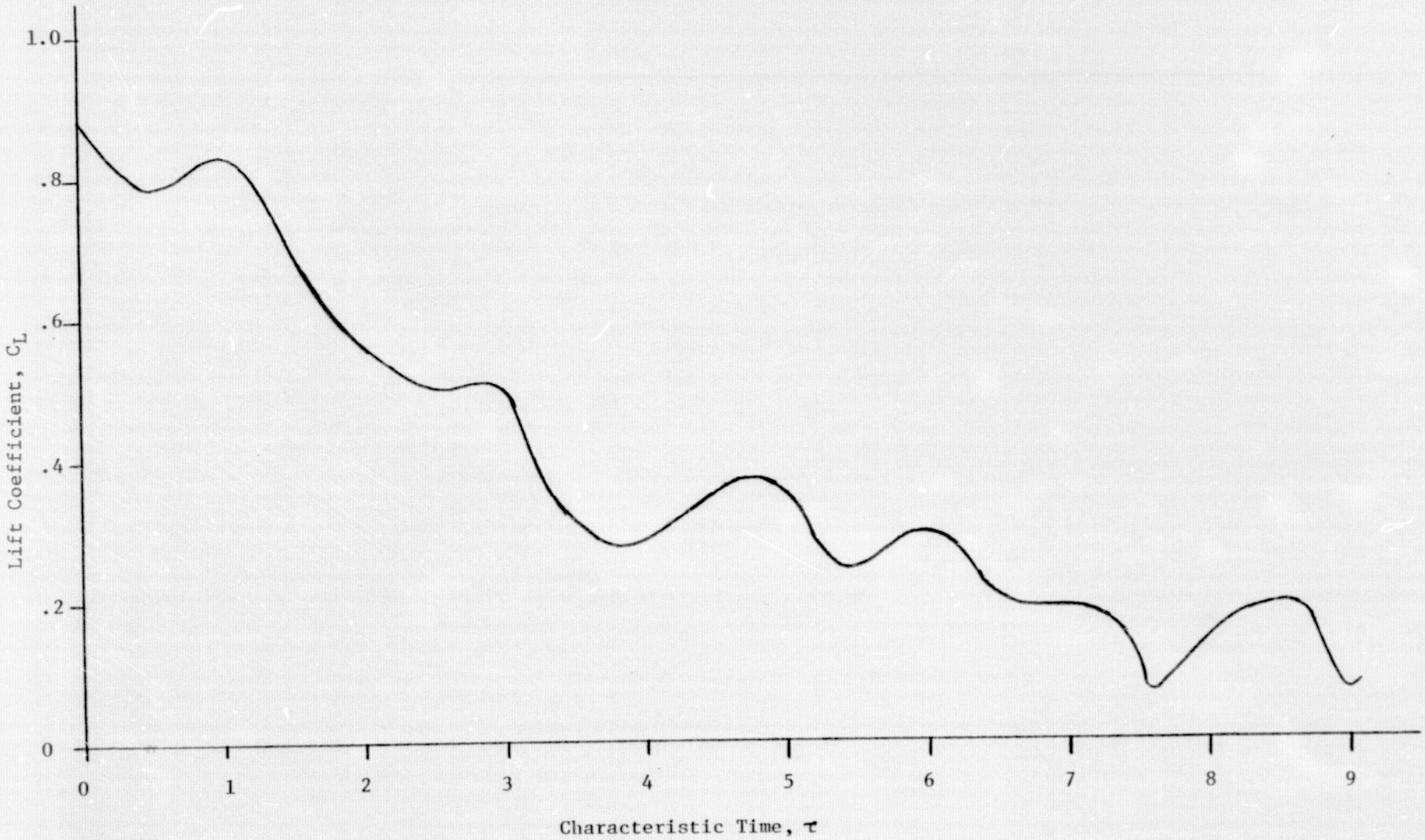


Figure 18. Time history of the lift coefficient for the NACA 64A010 airfoil at two-degrees angle of attack; Problem 102.0-medium mesh calculation; $M_\infty = .80$, $Re_{\infty c} = 4 \times 10^6$.

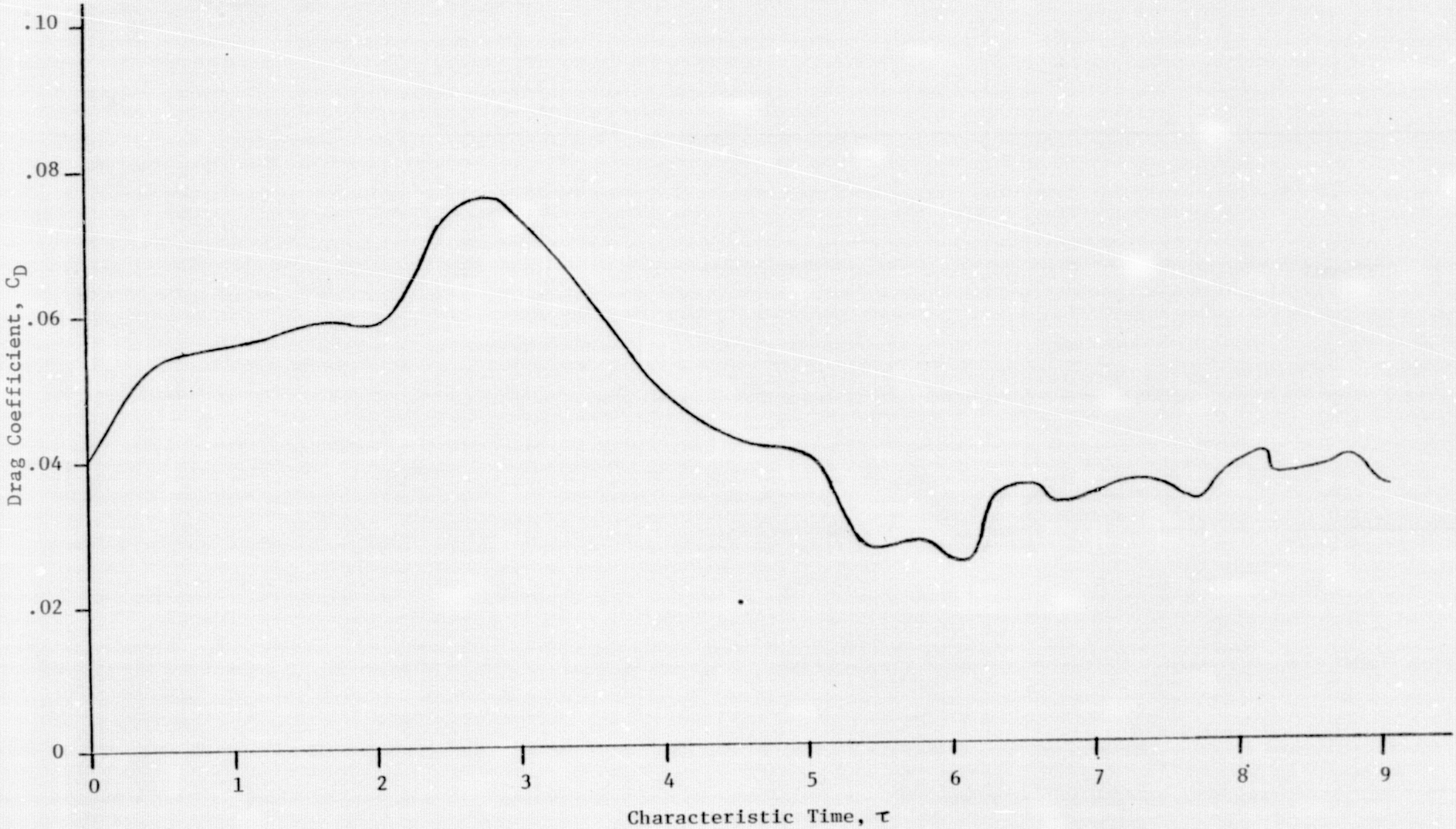


Figure 19. Time history of the drag coefficient for the NACA 64A010 airfoil at two degrees angle of attack; Problem 102.0 - medium mesh calculation, $M_\infty = .80$, $Re_{\infty c} = 4 \times 10^6$.

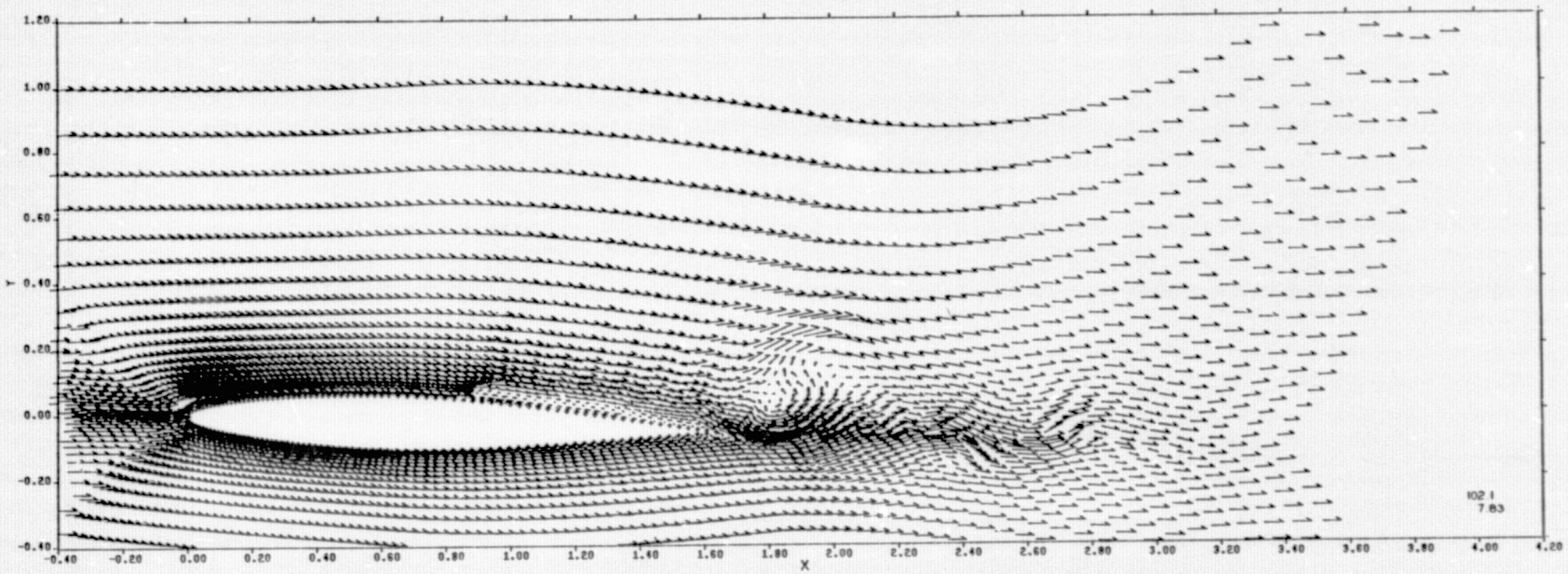


Figure 20. Velocity vector plot of the NACA 64A010 airfoil flow field at a characteristic time of 7.83; $M_\infty = .80$, $\alpha = 2^\circ$; $Re_{c_\infty} = 4 \times 10^6$; Problem 102.1

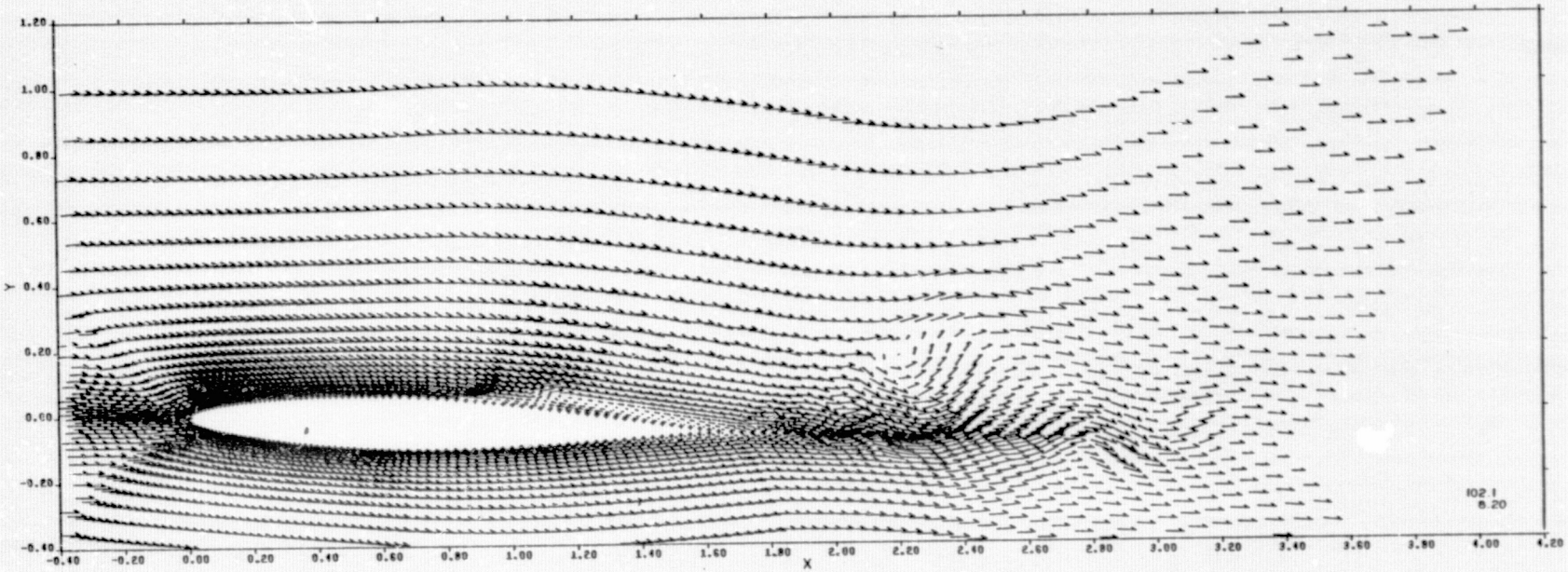


Figure 21. Velocity vector plot of the NACA 64A010 airfoil flow field at a characteristic time of 8.20; $M_\infty = .80$, $\alpha = 2°$, $Re_{c_\infty} = 4 \times 10^6$; Problem 102.1.

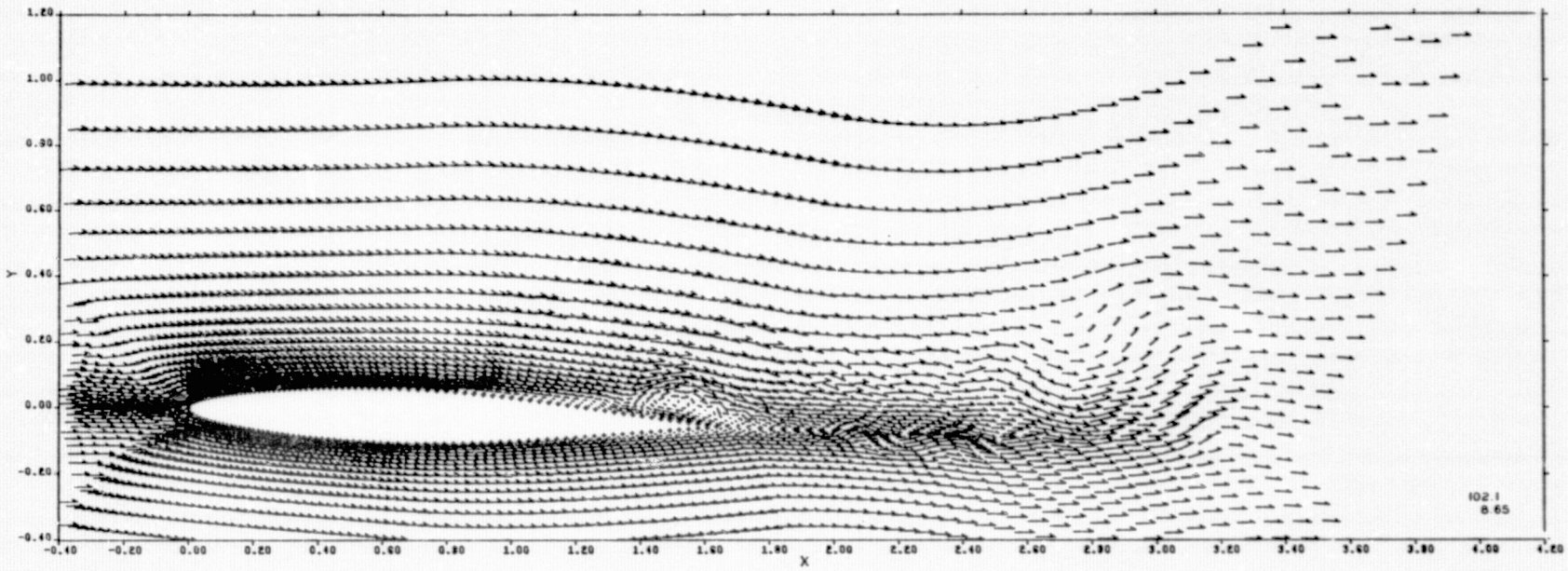


Figure 22. Velocity vector plot of the NACA 64A010 airfoil flow field at a characteristic time of 8.65; $M_\infty = .80$, $\alpha = 2^\circ$, $Re_{c_d} = 4 \times 10^6$; Problem 102.1

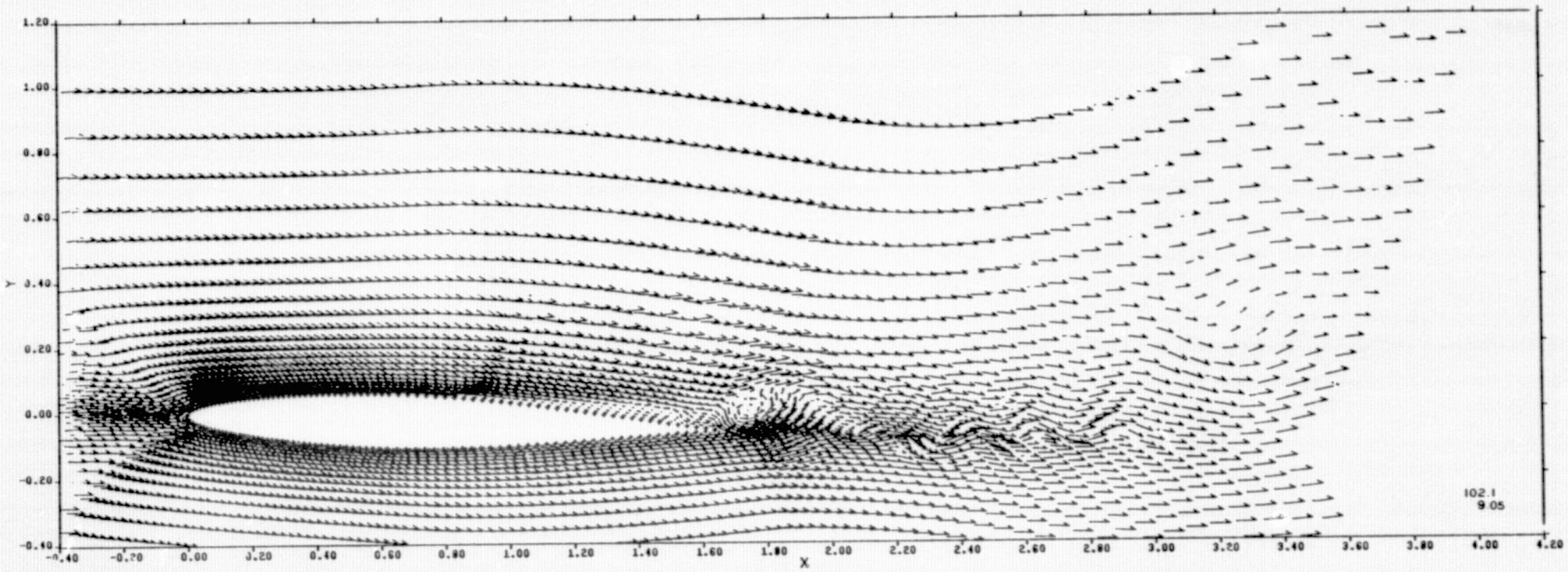


Figure 23. Velocity vector plot of the NACA 64A010 airfoil flow field at a characteristic time of 9.0; $M_\infty = .80$; $\alpha = 2^\circ$; $Re_{c_\infty} = 4 \times 10^6$; Problem 102.1.

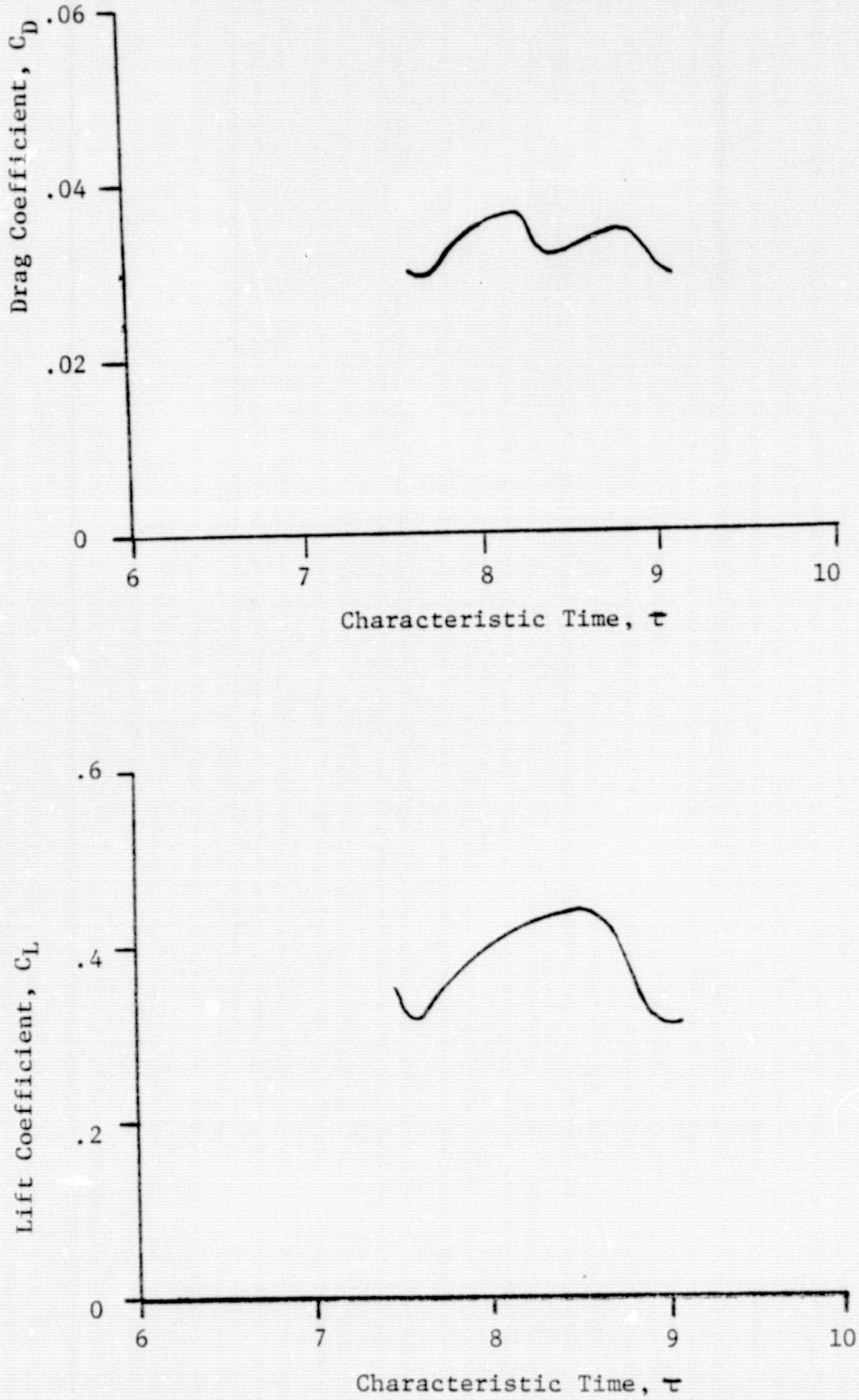


Figure 24. Time histories of the lift and drag coefficients for the NACA 64A010 airfoil at two degrees angle of attack; Problem 102.1 - integrated inviscid/viscous calculation; $M_\infty = .80$, $Re_{\infty_c} = 4 \times 10^6$.

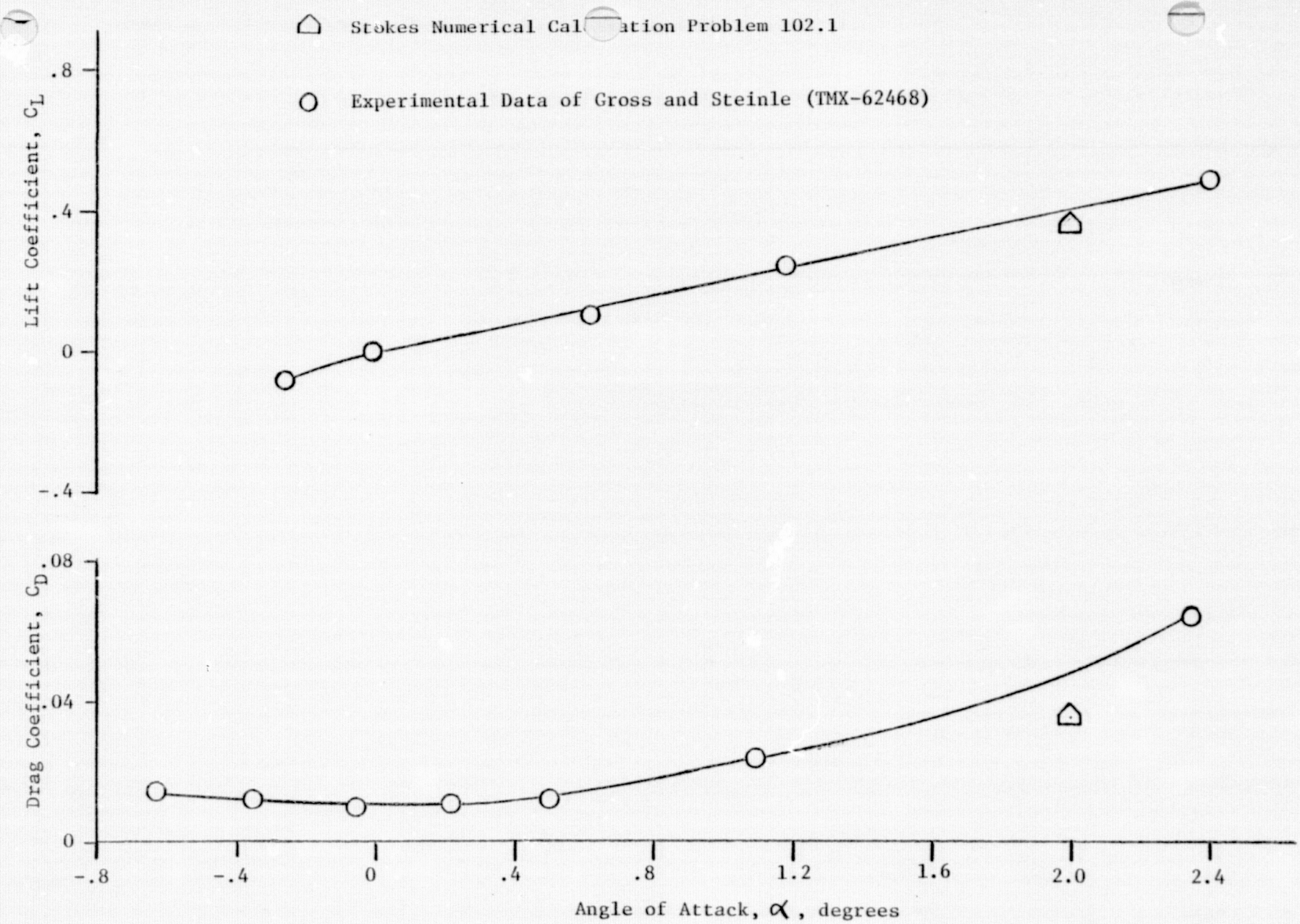


Figure 25. Comparison of numerically calculated time averaged lift and drag coefficients with corresponding experimental data; $M_\infty = .80$, $Re_{\infty c} = 4 \times 10^6$.

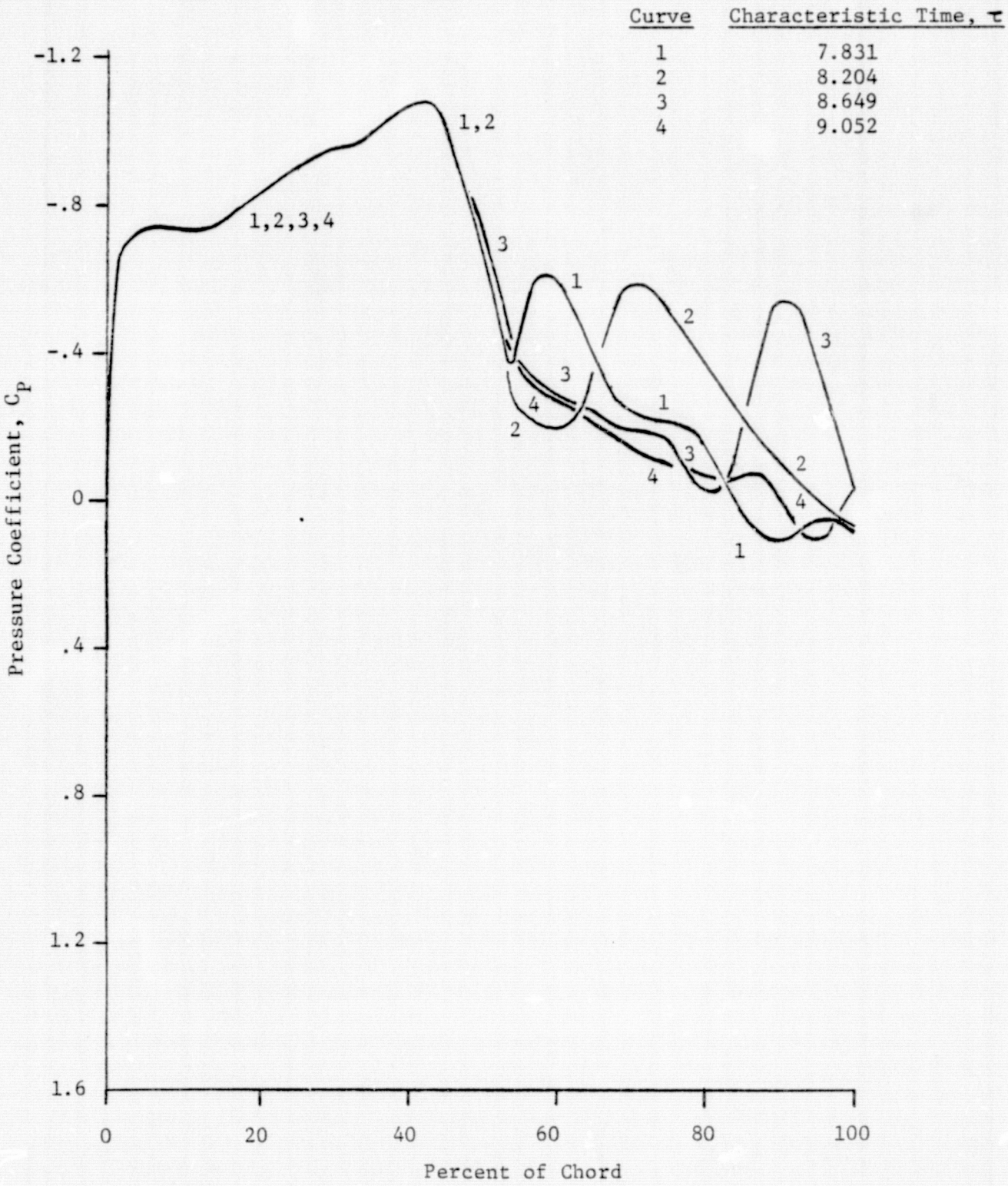


Figure 26. Pressure Coefficient distributions on the leeward surface of the NACA 64A010 airfoil; $M_\infty = .80$, $Re_{\infty c} = 4 \times 10^6$, $\alpha = 2°$; Problem 102.1.

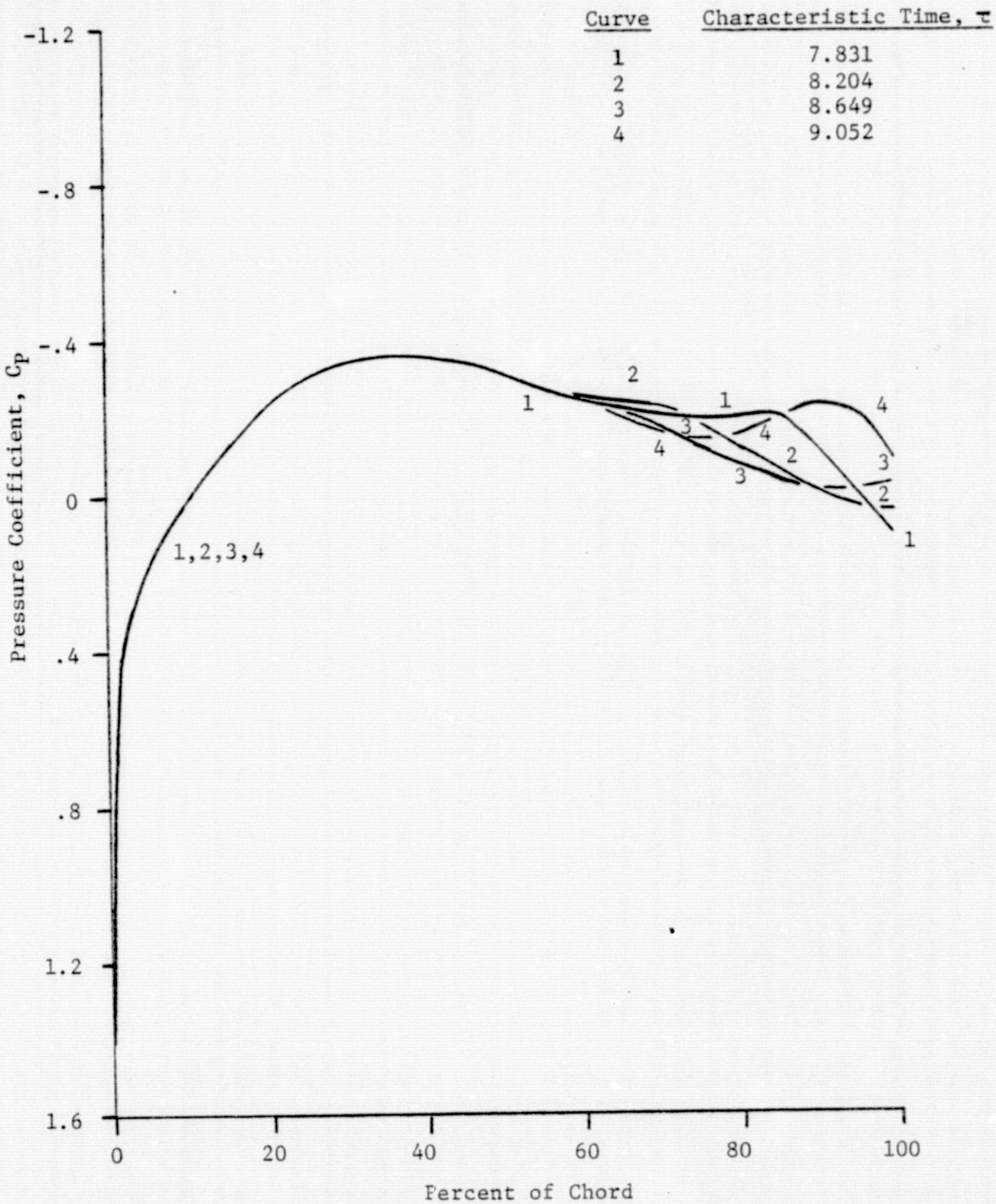


Figure 27. Pressure coefficient distributions on the windward surface of the NACA 64A010 airfoil; $M_\infty = .80$, $Re_{\alpha c} = 4 \times 10^6$, $\alpha = 2°$; Problem 102.1.

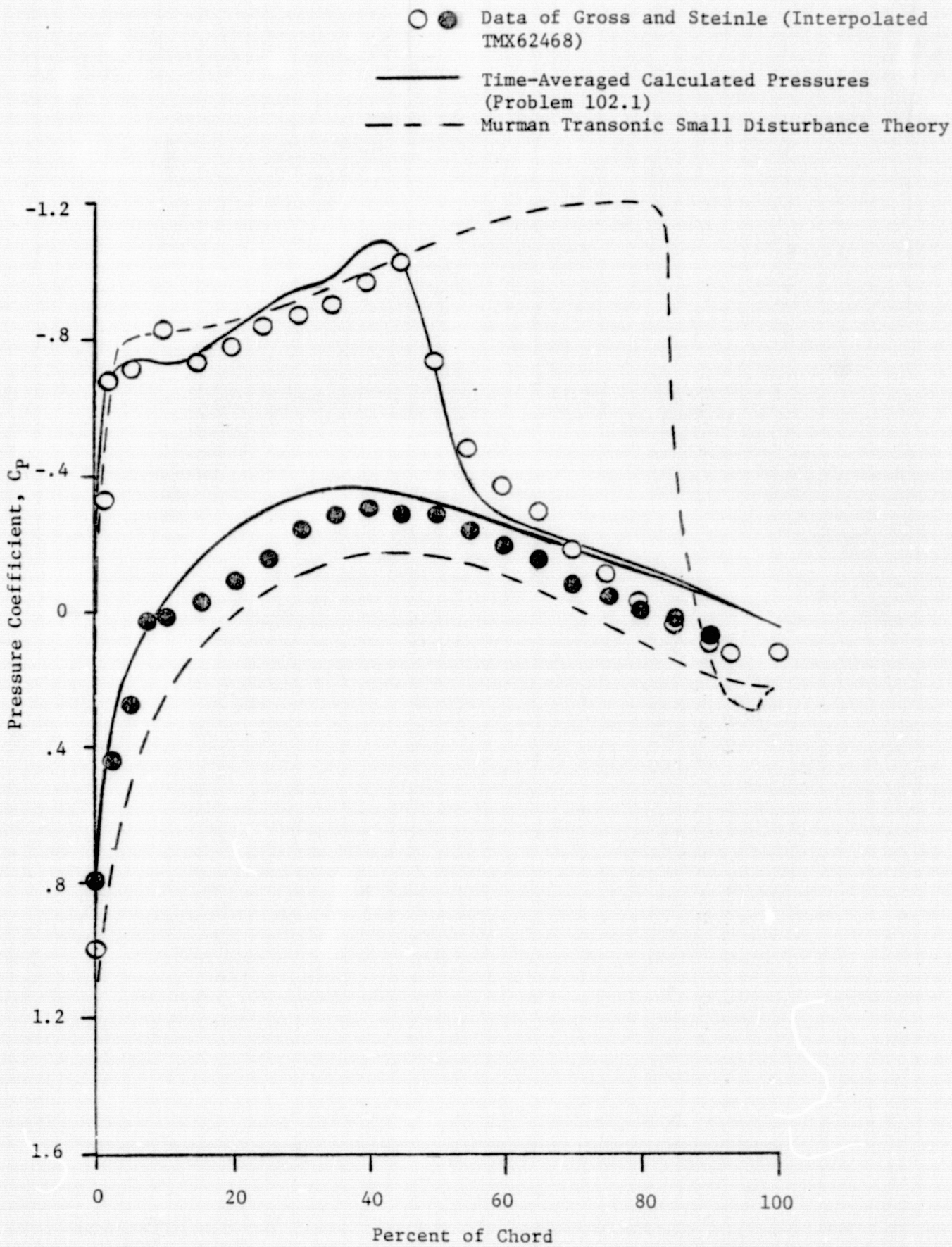


Figure 28. Comparison of calculated pressures with experimental data and transonic small disturbance theory; $M_\infty = .80$, $Re_{\infty_c} = 4 \times 10^6$, $\alpha = 2°$.

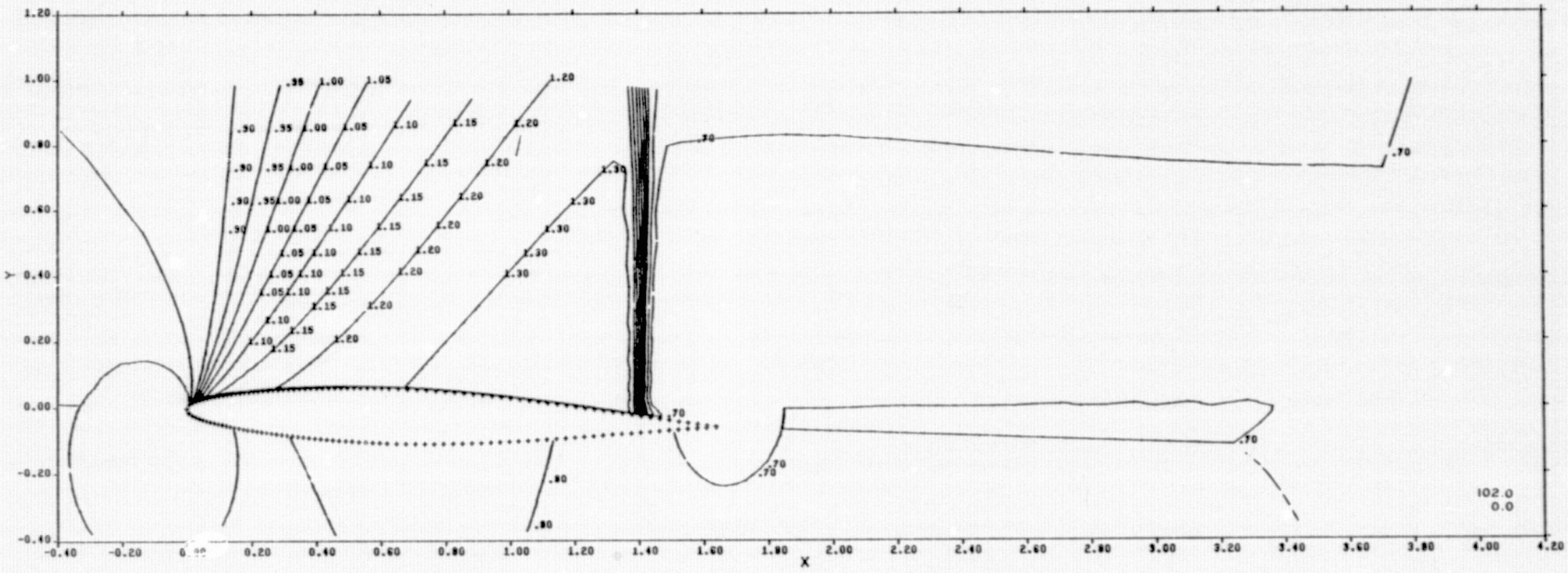


Figure 29. Mach number contours about the NACA 64A010 airfoil at two-degrees angle-of-attack based on the Murman-Cole inviscid solution; $M_\infty = .80$.

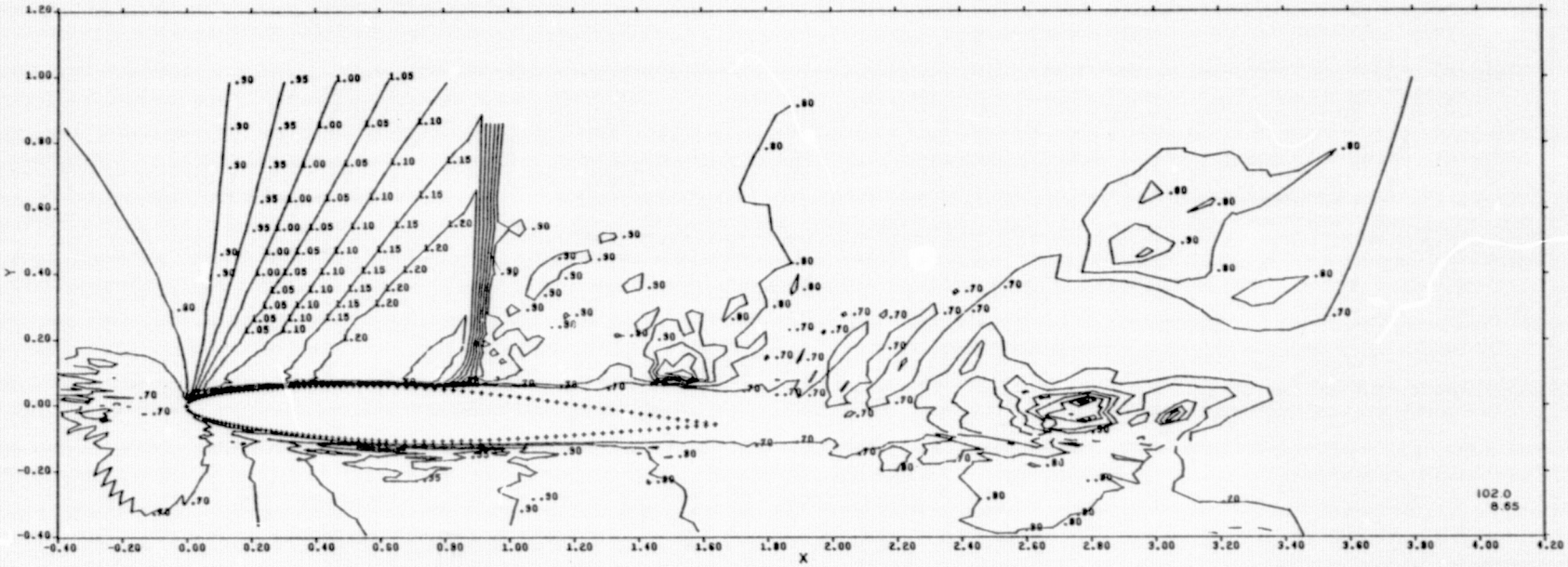


Figure 30. Mach number contours about the NACA 64A010 airfoil at two degrees angle-of-attack and at a characteristic time of 8.65; $M_\infty = .80$, $Re_{c_\infty} = 4 \times 10^6$; Problem 102.1.

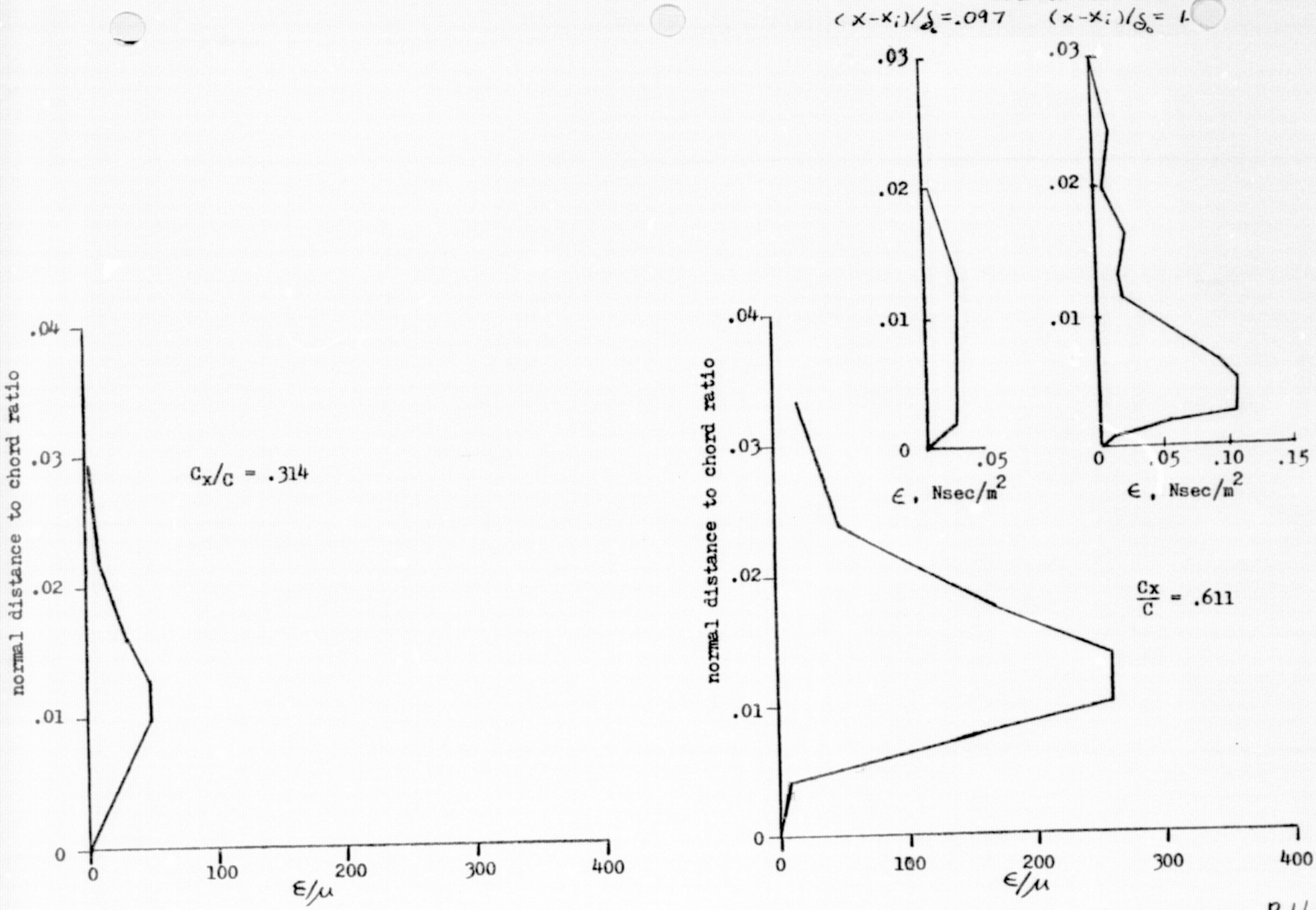


Figure 31. Profiles of $\epsilon/\mu$ upstream of and downstream of the leeward shock wave on the NACA 64A010 airfoil; Problem 102-1.